Filament formation by glutaminase enzymes drives catalysis

Shi Feng[1], Cody Aplin[1], Thuy-Tien T. Nguyen[1] and Richard A. Cerione[1,2*]

[1]Department of Chemistry and Chemical Biology, Cornell University, Ithaca, New York, 14853
[2]Department of Molecular Medicine, Cornell University, Ithaca, New York, 14853

ABSTRACT

The mitochondrial glutaminase enzymes initiate glutaminolysis by catalyzing the hydrolysis of glutamine to glutamate, satisfying the metabolic requirements of aggressive cancers and thus representing potential therapeutic targets. However, the mechanisms underlying their allosteric regulation are poorly understood. It has been suggested that glutaminases form oligomeric filament-like structures essential for their activation. Here, we provide structural evidence for the ability of the glutaminase enzymes to form filaments upon substrate binding, and present the first cryo-EM structures of the human full-length glutaminase isozyme GLS2 that offer an unprecedented view of the mechanism responsible for catalyzing glutamine hydrolysis. The GLS2 structures reveal that the 'activation loop', a motif previously identified to regulate enzymatic activity, assumes a unique conformation and works together with a 'lid' that closes over the active site to 'lock in' the substrate glutamine. Tyrosine 251 of the GLS2 activation loop forms a cation-π interaction with Lysine 222 in the active site, which in turn enables a key catalytic residue, Serine 219, to undergo deprotonation for nucleophilic attack on the substrate. These findings further suggest that allosteric glutaminase inhibitors disrupt this interaction, which is critical for catalysis, while activators stabilize it. The GLS2 structures also show how the ankyrin repeats regulate different glutaminase isozymes.

INTRODUCTION

Metabolic reprogramming is well-established as a hallmark of cancer progression [1-3]. A shift in the metabolic requirements of cancer cells compared to normal cells, known as the Warburg effect [4-6], results in their dependence on glutamine as an energy source in addition to glucose. Glutamine catabolism, which starts with the hydrolysis of glutamine to glutamate, catalyzed by the glutaminase family of enzymes, becomes highly upregulated in cancer cells to compensate for the uncoupling of the glycolytic pathway from the TCA cycle due to the Warburg effect, thus providing the biosynthetic precursors necessary for their enhanced proliferation and survival [7-10]. Given the resulting 'glutamine addiction' of cancer cells, the development of allosteric small molecule inhibitors that target glutaminase activity is being examined as a potential therapeutic strategy [11-13] to block tumor progression in aggressive breast, lung, and pancreatic cancers, as well as various other malignancies. The glutaminases are encoded by two independent genes, GLS and GLS2. GLS encodes kidney-type glutaminase (KGA) and its C-terminal truncated splice variant glutaminase C (GAC), the predominant form of GLS expressed in many cancers, while GLS2 is expressed as only one active isozyme, liver-type glutaminase (LGA). All glutaminase enzymes share a catalytic domain containing identical active site residues and a conserved mechanism for hydrolyzing glutamine to glutamate [14-16]. The catalytic efficiency of all glutaminase enzymes is markedly increased in the presence of inorganic phosphate *in vitro* [17, 18], but the concentration of this allosteric activator required to activate these enzymes is unattainable in most physiological contexts. Thus, there is still a good deal to learn regarding the identity of the actual physiological activators of glutaminases, particularly the structural changes induced by these activators necessary to achieve catalysis. Understanding more about the catalytic mechanism used by these enzymes will be especially important for further developing drug candidates that effectively block their enzymatic activity. Even though potent inhibitors targeting GAC are available, the most effective being

the BPTES/CB-839 group of compounds [19, 20] with CB-839 and others having nanomolar binding affinity, the development of specific and potent allosteric inhibitors of GLS2 has not been as successful, as currently, the best examples are the 968-class of molecules [9, 21] which have binding affinities for the enzyme only in the micromolar range.

Recently it has been shown that GAC can assemble into long filaments in cells to facilitate efficient glutamine consumption [22]. The formation of these oligomeric supramolecular assemblies has also previously been associated with the *in vitro* activation of GAC by inorganic phosphate [23, 24]. However, whether filament formation is a common mechanism for all glutaminase isozymes, and if the assembly of such higher-order oligomers is directly coupled to catalytic activity, have yet to be established. In addition, it has been suggested that KGA, GAC, and GLS2 are differentially regulated due to the presence of ankyrin repeats on specific isozymes [25]. Ankyrin repeats are one of the most common protein structural motifs and are typically involved in mediating protein-protein interactions [25, 26]. Thus, their presence in different glutaminase enzymes (i.e., KGA and GLS2) might be essential for regulating catalytic activity. In this study, we show that both GAC and GLS2 undergo filament formation in the presence of the substrate glutamine and the activator inorganic phosphate, with the assembly of this higher-order oligomer being tightly coupled to glutamine hydrolysis and product (glutamate) release. We further present a high-resolution structure for a glutaminase filament (GLS2) determined by cryo-electron microscopy (cryo-EM). This novel filamentous structure provides essential insights into the catalytic mechanism used by the glutaminase enzymes and sheds new light on how the ankyrin repeats regulate enzymatic activity.

RESULTS

Structural characterization of full-length wildtype GLS2

While there have been several high-resolution X-ray structures for different forms of GLS, thus far, there has not been a structural determination for the full-length GLS2 protein (also known as liver-type glutaminase or LGA). Therefore, we obtained a cryo-EM structure for the wildtype, full-length human apo-GLS2. Figs. 1A and 1B show the 3.1 Å structure of the GLS2 tetramer and the relative positions of the key regions for catalytic activity (i.e., the ‘activation loop’, the catalytic site, and the ‘lid loop’ that opens and closes over the catalytic domain) [16]. Fig. 1C shows the three major domains of a monomeric unit of GLS2, namely, the N-terminal region, C-terminal ankyrin repeats, and the highly conserved catalytic site. The overall structure of the apo-GLS2 tetramer strongly resembles those of the previously reported X-ray crystallography structures of the apo-forms of GAC and KGA (Fig. 1C, Fig. S1A) [17, 25].

The catalytic sites within each subunit of GLS2 show the same features as a previously reported crystal structure of the limit catalytic domain (Fig. 1D) [15]. These features are highly conserved throughout the glutaminase enzymes, including the GLS isoforms KGA and GAC, indicative of a shared catalytic mechanism for all members of the glutaminase family. We analyzed several critical structural elements in the catalytic domain of GLS2 that have previously been suggested to regulate glutaminase activity allosterically. The stretch of residues Gly248-Glu258, which has been shown to play an essential role in catalysis and thus referred to as the 'activation loop' [16, 27], is disordered and flexible in the GLS2 structure (Fig. 1B). In GAC, this loop contains the binding site for the BPTES class of allosteric inhibitors which includes CB-839, a drug candidate that has been in clinical trials [19]. The loop forms a stable, inactive conformation when bound to BPTES and to its more potent analogs, such as CB-839 (not shown) and UPGL0004 (Fig. S1B) [28]. However, the activation loop of GLS2 differs from KGA and GAC by two residues, rendering GLS2 insensitive to these inhibitors [17]. In addition, residues Tyr182-Lys188 in GLS2, which correspond to a loop in KGA and GAC that forms a 'lid' that needs to close over bound substrates for catalysis to occur, are also flexible in the GLS2 structure. This is in contrast to the previously reported crystal structure of the GLS2 limit catalytic domain, which showed the lid region adopting an "open" conformation [15].

Glutaminase filament formation is coupled to catalytic activity

The glutaminase enzymes have been shown to undergo dimer-to-tetramer transitions upon binding activators such as inorganic phosphate (Pi) [18]. This transition has been suggested to be necessary for enzyme activity. However, high-resolution structures of the tetrameric form of glutaminase enzymes have failed to shed light on the critical changes in their catalytic sites that promote the hydrolysis of glutamine to glutamate. In fact, the positions of the catalytic residues in the structures obtained for glutaminase dimers and tetramers are virtually identical. Therefore, there have been suggestions that GAC needs to form a higher-order oligomeric state in cells, resulting in a filament-like structure, in order for catalysis to occur [22, 24, 29]. Given the structural similarities between GAC and GLS2, it might be expected that GLS2 would undergo a similar structural transition. Therefore, we set out to see if a filament-like structure is indeed formed by all glutaminase enzymes and whether its formation is coupled to catalysis.

Using negative-stain electron microscopy (EM), we visualized the structural changes that recombinant human GLS2 undergoes in the presence of the substrate glutamine and the anionic activator Pi, i.e., under catalytic conditions. We found that in the presence of glutamine and Pi, GLS2 immediately assembled into filamentous structures (Fig. 2A). However, within approximately 10 minutes, when the substrate glutamine was fully converted to product (glutamate), the GLS2 filaments disassembled into tetramers (Fig. 2B), thus supporting the idea that filament formation is coupled to catalysis. We also visualized human GAC in the presence of glutamine and Pi and observed filaments similar to GLS2 (Fig. 2C), further indicating that filament formation is common to all glutaminase enzymes.

To further establish a direct connection between filament formation and enzyme catalysis, we took advantage of right-angle light scattering (RALS) to monitor their assembly in real time. As shown in Fig. 2D, upon adding Pi and glutamine to GLS2, there was an immediate, marked increase in light scattering. The increase in RALS peaked in minutes and was followed by a rapid decline, and the persistence of the peak matched the time scale for dissociation of GLS2 filaments as visualized by negative-stain EM. The maximal increase in RALS required both the substrate glutamine and the anionic activator Pi and was not detected in the absence of substrate (Fig. S2A). These results strongly suggest that the changes in RALS accurately reflect the association and dissociation of GLS2 filaments. Subsequent additions of glutamine to GLS2 re-established filament formation, with substrate consumption again resulting in filament disassembly (Fig. 2D). The addition of the product, glutamate, was unable to trigger filament formation. Taken together, these results further demonstrate that filament formation is directly coupled to substrate binding and catalytic activity.

Mutations that result in the constitutive activation of the glutaminase enzymes were then examined by negative-stain EM and RALS for their effects on filament formation. We previously found that changing a key lysine residue (i.e., Lys320 in GAC and Lys253 in GLS2) to an alanine within the activation loop gives rise to constitutively active enzymes, with their activity matching that of the wildtype enzyme in the presence of Pi [30]. The RALS profile and negative-stain images showed that glutamine addition alone was sufficient to drive constitutively active forms of human GAC (K320A) and GLS2 (K253A) to form filaments, as the activation loop substitution effectively substitutes for the need of an anionic activator (Figs. S2B-S2D). Again the product glutamate was unable to drive filament assembly, nor did the presence of high concentrations of glutamate prior to glutamine addition have any affect on the ability of substrate to induce filament formation (Fig. S2D). We also examined a substitution of an essential tyrosine residue within the enzyme active site of GAC, which enables substrate (glutamine) binding but prevents its hydrolysis to glutamate. As shown in Fig. 2E, the RALS signal for GAC (Y466W) did not diminish over time, thus further reinforcing the conclusion that filament formation is directly correlated with the activated state of the enzyme.

143 **Structural determination of a GLS2 filament**

144 To capture the structure of the GLS2 enzyme under catalytic turnover conditions, we obtained a cryo-
145 EM structure of the recombinant human GLS2 (K253A) mutant in the presence of substrate. The 3.3 Å
146 structure, obtained prior to substrate depletion, enabled us to visualize an activated glutaminase filament
147 for the first time (Figs. 3A, B). The GLS2 (K253A) filaments can consist of as many as 30 tetramers, whose
148 length is directly proportional to the substrate concentration (Figs. 3C, S2E). The tetramers are arranged
149 in a side-by-side architecture, and each successive tetramer is rotated ~45 degrees relative to the filament
150 axis (Fig. 3B).

151 We also obtained a 6 Å 3D reconstruction of the mouse GAC (Y471W) mutant, which like the human
152 GAC (Y466W) mutant binds substrate but is defective for hydrolyzing glutamine [18] and assembles into
153 a filament similar to that of GLS2 [18](Fig. S3). These results contrast with the previously proposed end-
154 to-end double helix model for glutaminase filament formation [24]. In the GLS2 filament structure, each
155 tetramer interacts with its immediate neighbor through an interface of six alpha helices on the lateral side
156 of the catalytic domain near the lid loop that closes over the substrate binding site (Fig. 3D, left panel).
157 Within this interface, Phe288, Phe306, Phe311, Asp345, and Gln349 from one subunit form an intricate
158 interacting network with Arg308 and Gln312 from the subunit of an adjacent tetramer (Fig. 3D, right
159 panel).

160 When comparing the structure of the GLS2 filament with the tetrameric apo-enzyme (i.e., in the
161 absence of substrate), we found striking differences in the conformation of the activation loops and the
162 lids. The activation loops of tetrameric GLS2 and GAC, either in their apo-, substrate-bound, or product-
163 bound states, are highly flexible and cannot be resolved (Fig. 1B), except when GAC is bound to the BTPES
164 class of inhibitors (Fig. S1B). This led us to originally suspect that a flexible, rather than stabilized,
165 activation loop was essential for the catalytic activity of these enzymes. However, in the constitutively
166 active GLS2 filament structure, the activation loops are well resolved and adopt a conformation distinct
167 from the inhibitor-induced state in GAC (Figs. 3D, S1B).

168 The first significant conformational change involving the activation loops of the GLS2 filament
169 resulted in a new motif designated as the 'tyrosine lock'. In each dimer within a tetrameric unit of the
170 filament, Glu258 from the activation loop of one monomer subunit forms a new salt bridge with Arg250
171 from the activation loop of the adjacent monomer subunit (Fig. 4A). This new salt bridge allows the
172 activation loops of each dimer to compactly fold, thereby bringing Tyr251 from the activation loop closer
173 to the active site (Fig. 4A). The lid loops also undergo significant conformational changes resulting in
174 Tyr182 inserting into the active site pockets. Thus, these two rearrangements fully close off the active site
175 in each subunit as a 'tyrosine lock', effectively locking the substrate glutamine into an optimal orientation
176 proximal to the residues essential for catalysis (Fig. 4B). The insertion of the phenyl ring of Tyr251 brings
177 it within ~5 Å of Lys222 (Fig. 4C), enabling a cation-π interaction that orients and increases the basicity of
178 Lys222. In the first step of catalysis, Lys222 can now effectively deprotonate Ser219, which undergoes a
179 nucleophilic attack and forms a tetrahedral intermediate with glutamine. Hydrolysis can then occur
180 following this initial reaction to form glutamate and ammonia [31].

181 Another significant conformational change that occurs in the GLS2 filament structure results in a new
182 hydrogen bonding network introduced by the activation loops. Hydrogen bonds that form between
183 Arg250 and Asp400 appear to 'stretch' the alpha helix containing Asp400, causing Tyr399 on the N-
184 terminal end of the alpha helix to insert further into the active site where the substrate binds (Fig. 4A).
185 Following the insertion of Tyr399, Glu258 from the adjacent dimer forms a hydrogen bond with Lys440,
186 which displaces the loop containing Lys440, and therefore makes space for the insertion of Tyr399. As a
187 result, Tyr399 is now in close proximity to the substrate and Lys222, which is necessary for catalysis. These
188 unprecedented visualizations of the interactions within the active sites of the GLS2 filament under
189 catalytic turnover conditions provide fundamental new insights into the mechanisms by which the
190 glutaminase enzymes catalyze glutaminolysis.

When comparing the GLS2 filament with the apo-structure, we also observed the formation of a new salt bridge between Arg320 and Glu330 from the subunit of an adjacent dimer within the dimer-dimer interface of a tetrameric unit of the GLS2 filament (Fig. S4A). In apo-GLS2, Arg320 faces toward the active site and blocks the formation of the tyrosine lock. In the filament structure of activated GLS2 (K253A), Tyr182 is stabilized, causing Arg320 to adopt a new conformation and form a salt bridge with Glu330 at the dimer-dimer interface. This salt bridge may be necessary for the glutaminase enzymes to undergo the dimer-to-tetramer transition, which is a prerequisite for filament formation and catalytic activity. In addition, the putative position of Lys253, as inferred by the location of the alanine residue in the GLS2 (K253A) mutant, also suggests a putative binding site for anionic activators like Pi within the activation loops. The amide backbones of the mutant Ala253 residues in adjacent activation loops are separated by 17 Å, and both of the alanine side chains face inward, toward the center of the tetramer. Given the length of the lysine side chain (~6 Å) and the diameter of a phosphate molecule (~ 2.3 Å), the positively charged Lys253 could interact with the negatively charged phosphate to form a triad with Lys253 from an adjacent subunit, thereby stabilizing the activation loops in the active conformation (Fig. S4B). Conversely, in the absence of phosphate and substrate, the activation loops of the enzyme are flexible and, thus, not visualized.

A mechanism for glutaminase activation

The high-resolution GLS2 filament structure and RALS data presented here show how glutaminase filament formation is coupled to catalysis. In apo-GLS2, the lid does not adopt a fixed conformation and is highly flexible (Fig. 1B). Such flexibility would likely introduce steric clashes at the tetramer-tetramer interfaces within the GLS2 filament, thereby preventing filament formation (Fig. 5A). Upon binding to the active site, the substrate forms hydrogen bonds with Glu314, resulting in the movement of Glu314 toward the active site. The hydrogen bond enables the alpha helix containing residues Asn308 to Thr317 to move inward, resulting in additional interactions between Thr310 and Gln185, and between Ser313 and Pro184 on the lid loop, forming a 'secondary lock' (Fig. 5B). These two sets of interactions, and that which occurs between Tyr182 and the substrate, stabilize the lid in a conformation to form the tyrosine lock with Tyr251 from the activation loop. The tyrosine lock closes over the substrate and enables catalysis to occur, as well as exposes the filament interface, thus allowing additional tetramers to contribute to the growth of the higher-order oligomer (Fig. 5A). Reciprocally, it is the binding of tetramers to form the enzyme filament that restricts the flexibility of lids and to adopt a conformation that closes over the substrate sites for enzymatic activity. Following a catalytic turnover, the product glutamate has a relatively low affinity for the enzyme and no longer interacts with Tyr182 and Glu314. Upon the dissociation of product, the activation loops and the lids becoming highly flexible again to await the next substrate binding event. When all the available substrate is consumed, the lids are not able to be restrained, which disrupts the filament interface and gives rise to the dissociation of the filament back to tetramers (Fig. 5A). The missing density of the lid loop of the terminal tetramer in the cryo-EM map for the GLS2 (K253A) filament represents a snapshot of this detachment (Fig. 5C), consistent with our other results indicating that the filament dissociates upon substrate consumption.

The role of the ankyrin repeats in GLS2 and the longer GLS species KGA

The C-terminal region of GLS2 contains an ankyrin repeat motif consisting of three pairs of helical bundles located on the distal ends of the tetramer. The ankyrin repeats in GLS2 appear to exert a negative regulation of catalytic activity, despite being approximately 70 Å away from the active sites in each subunit. The KGA isoform of GLS also contains ankyrin repeats and has a much lower specific activity than its C-terminal truncated splice variant GAC which lacks these motifs; morever, truncated forms of KGA lacking these repeats show increased specific activity [25]. Each GLS2 dimer within a tetramer shares an ankyrin repeat bundle connected to the catalytic domain through a flexible linker. Interestingly, the

239 ankyrin repeats are highly asymmetric. Instead of showing symmetric occupancy of the area between the
240 N-terminal motifs of adjacent monomeric units within a tetramer, they show a preferential occupancy on
241 one particular side (Fig. S5). The presence of the ankyrin repeats results in a wider angle between
242 monomers in each GLS2 dimer within the apo-enzyme tetramer when compared to their positions in
243 crystal structures of KGA and GAC (Fig. 1C). In the GLS2 filament structure under catalytic conditions, the
244 activation loops within each tetrameric unit need to move into close proximity and to form a salt bridge
245 between Arg250 and Glu258 that enables them to be correctly positioned for catalytic activity (Fig. 6A,
246 supplementary movie S1). However, within the apo-GLS2 structure, the ankyrin repeats appear to hinder
247 this movement and thereby prevent the activation loops from adopting the positions necessary for
248 maximal catalytic capability (Fig. 6B). These effects may account for GLS2 having a lower specific activity
249 compared to GAC which lacks ankyrin repeats.
250
251
252 **DISCUSSION**
253 Members of the glutaminase family of enzymes have received significant attention as potential
254 therapeutic targets against aggressive cancers since they play a critical role in satisfying the glutamine
255 addiction exhibited by cancer cells [5, 19, 32-35]. This arises from their ability to catalyze the first step in
256 glutamine metabolism, the hydrolysis of glutamine to glutamate. GLS, particularly its carboxyl-terminal
257 splice variant GAC, and GLS2 have been implicated in cancer progression due to the upregulation of their
258 expression and catalytic activities [9, 35]. GAC expression is highly upregulated in basal-subtype (triple-
259 negative) breast cancer, while GLS2 is preferentially overexpressed in luminal-subtype (receptor-positive)
260 breast cancer [9]. The elevations in glutamine metabolism triggered by these metabolic enzymes serve to
261 compensate for the uncoupling of glycolysis from the TCA cycle, known as the Warburg effect, by
262 providing the carbon sources necessary for the biosynthetic processes that enable cancer cells to undergo
263 rapid proliferation and survive various types of cellular stress that would otherwise kill normal healthy
264 cells.
265 Various glutaminase inhibitors have been developed and characterized, including allosteric inhibitors
266 of the 968 class and the BPTES series of compounds [19, 21, 28, 35-37]. The latter includes CB-839, a
267 higher potency analog of BPTES, which has been examined in several clinical trials [19]. The BPTES class
268 of inhibitors has been shown to bind at an interface that forms when two dimers of GAC come together
269 to form a tetramer and acts by stabilizing the activation loop that is present within each subunit at the
270 dimer-dimer interface [36]. However, exactly how the stabilization of the activation loop by these
271 inhibitors prevents catalytic activity has not been well understood. This question has motivated our efforts
272 to learn more about the underlying mechanisms by which the glutaminase enzymes catalyze glutamine
273 hydrolysis. With that goal in mind, we have developed fluorescence spectroscopic readouts to monitor
274 directly the binding of the substrate glutamine in the presence and absence of the anionic activator Pi, as
275 well as monitor the interactions of allosteric inhibitors while simultaneously assaying enzyme activity [20,
276 30, 38, 39]. We have complemented these assays with structural determinations of GAC and GLS2, initially
277 using X-ray crystallography [18, 30, 36] and now cryo-EM. Our studies of GAC showed how the binding of
278 substrate and anionic activators helped to drive the transition between enzyme dimers to tetramers [18].
279 Interestingly, the binding of the substrate alone to GAC exhibited positive cooperativity and formed
280 asymmetric tetramers as viewed by X-ray crystallography. In contrast, in the presence of Pi, substrate
281 binding was equal and independent, with the enzyme subunits forming symmetrical tetramers in the X-
282 ray crystal structures [18]. Given that the addition of an anionic activator like Pi was necessary for enzyme
283 activity, it was assumed that the dimer-to-tetramer transition for the glutaminase enzymes was
284 responsible for catalysis. However, it was puzzling that when comparing the active sites for the dimeric
285 and tetrameric GAC species, there were no apparent differences in the positioning of the key catalytic
286 residues, nor was there any indication of how the activation loops contributed to enzyme activity. The

activation loops typically were disordered and thus not visualized in the structures, except in GAC complexes bound to the BPTES class of inhibitors.

A key to solving this puzzle came from our studies of the 3D structure of a constitutively active GLS2 mutant by cryo-EM. This mutant contained a Lys-to-Ala substitution within the activation loop that essentially mimics the actions of anionic activators like Pi under catalytic turnover conditions. Our initial intention was to see how similar the structure of GLS2 was to GAC, and particularly their active sites. However, we found that activated GLS2 forms higher-order filament-like structures comprising several enzyme tetramers under catalytic turnover conditions. Perhaps most importantly, the lifetime of the filaments was directly coupled to catalysis, as they persisted as long as sufficient substrate was available but then rapidly dissociated when the substrate was ultimately used up. We took advantage of a real-time assay for filament formation using right-angle light scattering and found that when examining wildtype GLS2 in the presence of both the substrate glutamine and the anionic activator Pi, the formation and dissolution of GLS2 filament formation matched catalytic turnover. This was also the case for GAC, confirming suggestions from other studies that the formation of GAC filaments is linked to catalytic activity [22, 24, 29].

The cryo-EM structure of the active GLS2 filament bound to glutamine was obtained upon rapid cryo-cooling of the enzyme immediately following substrate addition (i.e., to preserve the filament), and has provided critical new insights into the catalytic mechanism. For all prior structures of the glutaminase isozymes, the activation loops were only visible when the enzymes were bound to allosteric inhibitors of the BPTES family of compounds. Thus, there were no indications from prior 3D structural determinations of how the activation loops play a critical role in enzyme catalysis, especially given their apparent distance from the active sites. Likewise, there was little indication of how the activation loops communicated with the lids that form over the bound substrate, which is a necessary event for enzyme catalysis. However, for the first time, we have addressed these questions by determining a high-resolution 3D structure of an activated GLS2 filament. Specifically, this structure now shows activation loops that are well resolved and move toward the active site of each enzyme subunit, positioning Tyr251 of GLS2 sufficiently close to the catalytically essential residue Lys222 to form a cation-π interaction, which de-protonates an active site serine residue, thus promoting its nucleophilic attack on the substrate glutamine catalysis. The filament structure also shows that the lids undergo conformational changes relative to their positions in the apo-enzyme (tetramer), resulting in the insertion of a key residue, Tyr182, into the active site. These changes effectively close off each active site, with the two tyrosine residues, Tyr251 and Tyr182, locking the substrate glutamine into the proper orientation for catalysis. Several additional hydrogen bonding interactions are evident within the filament structure that help stabilize the interactions between the tetrameric units, which are not seen in the cryo-EM structure of apo-GLS2, and enable Tyr251 from the activation loop to be inserted into the active site. Upon catalytic turnover, glutamate is generated, which has a relatively low affinity for the enzyme and therefore is no longer interacting with the tyrosine lock nor the secondary lock at the lid loop that closes over each catalytic site. Product release relieves constraints on the activation loops and introduces flexibility to the lid loops, which block the interface between tetramers and result in the dissociation of the GLS2 filament. The fact that these changes are coupled to the catalytic reaction accounts for the tight correlation between enzyme activity and filament formation/dissociation. The structure of the GLS2 filament also sheds light on how the presence of ankyrin repeats, as found in GLS2 and the GLS isoform KGA but not GAC, results in a decrease in enzyme activity. In particular, the ankyrin repeats prevent the activation loops from achieving their optimal positions to contribute to maximal catalytic activity.

Overall, achieving a high-resolution structure for a glutaminase filament now opens the way to several interesting lines of study. For example, we will want to see how different classes of allosteric inhibitors affect filament formation and consider new strategies that might be developed to block the formation of these higher-order oligomers. Identifying other potential activators of the glutaminase enzymes will also

be essential, as it is unlikely that the Pi levels necessary to stimulate enzyme activity and filament formation can be achieved under most physiological contexts. Finally, it will be interesting to see how post-translational modifications such as lysine succinylation, which occurs at specific sites on GAC and has been suggested to both promote enzyme activation by stimulating oligomer (tetramer) formation [22] and to enhance ubiquitination and degradation [40], affects filament formation.

REFERENCES

1. Pavlova, N.N. and C.B. Thompson, *The Emerging Hallmarks of Cancer Metabolism.* Cell Metab, 2016. **23**(1): p. 27-47.
2. Faubert, B., A. Solmonson, and R.J. DeBerardinis, *Metabolic reprogramming and cancer progression.* Science, 2020. **368**(6487).
3. Hanahan, D., *Hallmarks of Cancer: New Dimensions.* Cancer Discov, 2022. **12**(1): p. 31-46.
4. Warburg, O., *On the origin of cancer cells.* Science, 1956. **123**(3191): p. 309-14.
5. Vander Heiden, M.G., L.C. Cantley, and C.B. Thompson, *Understanding the Warburg effect: the metabolic requirements of cell proliferation.* Science, 2009. **324**(5930): p. 1029-33.
6. Lukey, M.J., W.P. Katt, and R.A. Cerione, *Targeting amino acid metabolism for cancer therapy.* Drug Discov Today, 2017. **22**(5): p. 796-804.
7. Yang, C., et al., *Glutamine oxidation maintains the TCA cycle and cell survival during impaired mitochondrial pyruvate transport.* Mol Cell, 2014. **56**(3): p. 414-424.
8. Leone, R.D., et al., *Glutamine blockade induces divergent metabolic programs to overcome tumor immune evasion.* Science, 2019. **366**(6468): p. 1013-1021.
9. Lukey, M.J., et al., *Liver-Type Glutaminase GLS2 Is a Druggable Metabolic Node in Luminal-Subtype Breast Cancer.* Cell Rep, 2019. **29**(1): p. 76-88 e7.
10. Mendez-Lucas, A., et al., *Identifying strategies to target the metabolic flexibility of tumours.* Nat Metab, 2020. **2**(4): p. 335-350.
11. Altman, B.J., Z.E. Stine, and C.V. Dang, *From Krebs to clinic: glutamine metabolism to cancer therapy.* Nat Rev Cancer, 2016. **16**(11): p. 749.
12. Harding, J.J., et al., *A Phase I Dose-Escalation and Expansion Study of Telaglenastat in Patients with Advanced or Metastatic Solid Tumors.* Clin Cancer Res, 2021. **27**(18): p. 4994-5003.
13. Shen, Y.A., et al., *Inhibition of glutaminolysis in combination with other therapies to improve cancer treatment.* Curr Opin Chem Biol, 2021. **62**: p. 64-81.
14. Katt, W.P., M.J. Lukey, and R.A. Cerione, *A tale of two glutaminases: homologous enzymes with distinct roles in tumorigenesis.* Future Med Chem, 2017. **9**(2): p. 223-243.
15. Ferreira, I.M., et al., *Structure and activation mechanism of the human liver-type glutaminase GLS2.* Biochimie, 2021. **185**: p. 96-104.
16. Nguyen, T.T., W.P. Katt, and R.A. Cerione, *Alone and together: current approaches to targeting glutaminase enzymes as part of anti-cancer therapies.* Future Drug Discovery, 2023 (in press).
17. DeLaBarre, B., et al., *Full-length human glutaminase in complex with an allosteric inhibitor.* Biochemistry, 2011. **50**(50): p. 10764-70.
18. Nguyen, T.T., et al., *High-resolution structures of mitochondrial glutaminase C tetramers indicate conformational changes upon phosphate binding.* J Biol Chem, 2022. **298**(2): p. 101564.
19. Gross, M.I., et al., *Antitumor activity of the glutaminase inhibitor CB-839 in triple-negative breast cancer.* Mol Cancer Ther, 2014. **13**(4): p. 890-901.
20. Milano, S.K., et al., *New insights into the molecular mechanisms of glutaminase C inhibitors in cancer cells using serial room temperature crystallography.* J Biol Chem, 2022. **298**(2): p. 101535.
21. Katt, W.P., et al., *Dibenzophenanthridines as inhibitors of glutaminase C and cancer cell proliferation.* Mol Cancer Ther, 2012. **11**(6): p. 1269-78.

383 22. Jiang, B., et al., *Filamentous GLS1 promotes ROS-induced apoptosis upon glutamine deprivation*
384 *via insufficient asparagine synthesis.* Mol Cell, 2022. **82**(10): p. 1821-1835 e6.
385 23. Cassago, A., et al., *Mitochondrial localization and structure-based phosphate activation*
386 *mechanism of Glutaminase C with implications for cancer metabolism.* Proc Natl Acad Sci U S A,
387 2012. **109**(4): p. 1092-7.
388 24. Ferreira, A.P., et al., *Active glutaminase C self-assembles into a supratetrameric oligomer that can*
389 *be disrupted by an allosteric inhibitor.* J Biol Chem, 2013. **288**(39): p. 28009-20.
390 25. Pasquali, C.C., et al., *The origin and evolution of human glutaminases and their atypical C-terminal*
391 *ankyrin repeats.* J Biol Chem, 2017. **292**(27): p. 11572-11585.
392 26. Li, J., A. Mahajan, and M.D. Tsai, *Ankyrin repeat: a unique motif mediating protein-protein*
393 *interactions.* Biochemistry, 2006. **45**(51): p. 15168-78.
394 27. Li, Y., et al., *The activation loop and substrate-binding cleft of glutaminase C are allosterically*
395 *coupled.* J Biol Chem, 2020. **295**(5): p. 1328-1337.
396 28. Robinson, M.M., et al., *Novel mechanism of inhibition of rat kidney-type glutaminase by bis-2-(5-*
397 *phenylacetamido-1,2,4-thiadiazol-2-yl)ethyl sulfide (BPTES).* Biochem J, 2007. **406**(3): p. 407-14.
398 29. Moller, M., et al., *Small angle X-ray scattering studies of mitochondrial glutaminase C reveal*
399 *extended flexible regions, and link oligomeric state with enzyme activity.* PLoS One, 2013. **8**(9): p.
400 e74783.
401 30. Li, Y., et al., *Mechanistic Basis of Glutaminase Activation: A KEY ENZYME THAT PROMOTES*
402 *GLUTAMINE METABOLISM IN CANCER CELLS.* J Biol Chem, 2016. **291**(40): p. 20900-20910.
403 31. Brown, G., et al., *Functional and structural characterization of four glutaminases from Escherichia*
404 *coli and Bacillus subtilis.* Biochemistry, 2008. **47**(21): p. 5724-35.
405 32. DeBerardinis, R.J., et al., *Beyond aerobic glycolysis: transformed cells can engage in glutamine*
406 *metabolism that exceeds the requirement for protein and nucleotide synthesis.* Proc Natl Acad Sci
407 U S A, 2007. **104**(49): p. 19345-50.
408 33. DeBerardinis, R.J., et al., *The biology of cancer: metabolic reprogramming fuels cell growth and*
409 *proliferation.* Cell Metab, 2008. **7**(1): p. 11-20.
410 34. Gao, P., et al., *c-Myc suppression of miR-23a/b enhances mitochondrial glutaminase expression*
411 *and glutamine metabolism.* Nature, 2009. **458**(7239): p. 762-5.
412 35. Wang, J.B., et al., *Targeting mitochondrial glutaminase activity inhibits oncogenic transformation.*
413 Cancer Cell, 2010. **18**(3): p. 207-19.
414 36. Huang, Q., et al., *Characterization of the interactions of potent allosteric inhibitors with*
415 *glutaminase C, a key enzyme in cancer cell glutamine metabolism.* J Biol Chem, 2018. **293**(10): p.
416 3535-3545.
417 37. McDermott, L., et al., *GAC inhibitors with a 4-hydroxypiperidine spacer: Requirements for potency.*
418 Bioorg Med Chem Lett, 2019. **29**(19): p. 126632.
419 38. Stalnecker, C.A., et al., *Mechanism by which a recently discovered allosteric inhibitor blocks*
420 *glutamine metabolism in transformed cells.* Proc Natl Acad Sci U S A, 2015. **112**(2): p. 394-9.
421 39. Stalnecker, C.A., J.W. Erickson, and R.A. Cerione, *Conformational changes in the activation loop of*
422 *mitochondrial glutaminase C: A direct fluorescence readout that distinguishes the binding of*
423 *allosteric inhibitors from activators.* J Biol Chem, 2017. **292**(15): p. 6095-6107.
424 40. Greene, K.S., et al., *SIRT5 stabilizes mitochondrial glutaminase and supports breast cancer*
425 *tumorigenesis.* Proc Natl Acad Sci U S A, 2019.
426 41. Suloway, C., et al., *Automated molecular microscopy: the new Leginon system.* J Struct Biol, 2005.
427 **151**(1): p. 41-60.
428 42. Morin, A., et al., *Collaboration gets the most out of software.* Elife, 2013. **2**: p. e01456.
429 43. Scheres, S.H., *RELION: implementation of a Bayesian approach to cryo-EM structure*
430 *determination.* J Struct Biol, 2012. **180**(3): p. 519-30.

44. Zheng, S.Q., et al., *MotionCor2: anisotropic correction of beam-induced motion for improved cryo-electron microscopy.* Nat Methods, 2017. **14**(4): p. 331-332.
45. Punjani, A., et al., *cryoSPARC: algorithms for rapid unsupervised cryo-EM structure determination.* Nat Methods, 2017. **14**(3): p. 290-296.
46. Bepler, T., et al., *Positive-unlabeled convolutional neural networks for particle picking in cryo-electron micrographs.* Nat Methods, 2019. **16**(11): p. 1153-1160.
47. Pettersen, E.F., et al., *UCSF ChimeraX: Structure visualization for researchers, educators, and developers.* Protein Sci, 2021. **30**(1): p. 70-82.
48. Croll, T.I., *ISOLDE: a physically realistic environment for model building into low-resolution electron-density maps.* Acta Crystallogr D Struct Biol, 2018. **74**(Pt 6): p. 519-530.
49. Liebschner, D., et al., *Macromolecular structure determination using X-rays, neutrons and electrons: recent developments in Phenix.* Acta Crystallogr D Struct Biol, 2019. **75**(Pt 10): p. 861-877.
50. Emsley, P., et al., *Features and development of Coot.* Acta Crystallogr D Biol Crystallogr, 2010. **66**(Pt 4): p. 486-501.
51. Williams, C.J., et al., *MolProbity: More and better reference data for improved all-atom structure validation.* Protein Sci, 2018. **27**(1): p. 293-315.

450 **METHODS**

451 Recombinant glutaminase expression and purification

452 An N-terminal His-tagged form of the full-length human liver-type glutaminase isoform GLS2 without
453 the mitochondrial localization sequence (residue 38-602) was cloned into the pET28a plasmid as
454 previously described [36]. Site-directed mutagenesis was performed using Phusion DNA polymerase
455 (NEB). Protein expression was carried out first by transforming constructs into *E. Coli* BL21 (DE3)
456 competent cells, which were then grown in LB media overnight with 50 µg/mL kanamycin. The starter
457 cultures were subsequently inoculated at ~1:100 ratio in 6 L cultures with the same antibiotic
458 concentration and left shaking at 37°C, 180 rpm for 3-4 hours until the OD600 reached between 0.6 and
459 0.8. The flasks were then chilled at 4°C for 1-2 hours before induction with 30 µM IPTG (isopropyl β-D-1-
460 thiogalactopyranoside) and shaking at room temperature (RT), 180 rpm for 16-18 hours. Cells were
461 collected by centrifugation at 5,000xg for 10 minutes and frozen before resuspension in 150 mL lysis buffer
462 (50 mM Tris-HCl pH 8.5, 500 mM NaCl, 10% glycerol), supplemented with protease inhibitor cocktail
463 (Roche). Cells were lysed with lysozyme and mechanical sonication, and DNase I was added to reduce the
464 mixture's viscosity. The soluble fractions were separated from the debris by ultra-centrifugation
465 (40,000xg, 45 minutes). The lysate was then loaded onto Co^{2+}-charged TALON resin (GoldBio), equilibrated
466 previously with the wash buffer (50 mM Tris-HCl pH 8.5, 10 mM NaCl, 10 mM imidazole). The protein that
467 bound to the column was washed with the wash buffer and eluted with wash buffer supplemented with
468 320 mM imidazole. Further purification was performed by anion exchange chromatography using
469 MonoQTM column (GE Healthcare) and size-exclusion chromatography using SuperdexTM 200 pg 16/600
470 column (GE Healthcare). Human and mouse GAC preparations were prepared as previously described [18].
471 Proteins were kept in 20 mM Tris-HCl pH 8.5, 150 mM NaCl, snap-frozen in liquid nitrogen, and stored at
472 -80°C. Protein concentrations were determined by absorbance at 280 nm using extinction coefficients
473 calculated using the Expasy ProtParam tool.

474

475 Right-angle light scattering (RALS)

476 Frozen glutaminase aliquots were thawed on ice and diluted to a final concentration of 2 µM in 1 mL
477 of gel filtration buffer (20 mM Tris-HCl pH 8.5, 150 mM NaCl) added in a 1.2 mL cuvette and inserted into
478 a Varian Cary Eclipse fluorimeter. The cuvette temperature was set to 25°C and stirred with a magnetic
479 stir bar. The signal was recorded using excitation and emission wavelengths of 340 nm (5 nm bandpass).
480 The samples were incubated until the signal was stable (~2-3 mins), then 100 µL of glutamine from a 200
481 mM stock solution were added to initiate the reaction. Subsequently, 100 µL of inorganic phosphate (1
482 M) or glutamate (200 mM) were added for further analysis. The raw scattering traces were filtered to
483 improve the signal-to-noise ratio using SciPy and plotted using Matplotlib.

484

485 Negative-stain Electron Microscopy

486 Formvar/carbon film 200 mesh copper grids (Electron Microscopy Sciences, EMS) were plasma
487 cleaned by using PELCO easiGlow system (TED PELLA). Glutaminase (final concentration: 1 µM) was mixed
488 with the substrate glutamine (final concentration: 20 mM). Inorganic phosphate (K_2HPO_4 final
489 concentration: 50 mM) was added to the mixture when needed. The mixture was incubated at RT for 30
490 seconds. Then, 10 µL of the mixture was applied onto the grids for a 60-second incubation, and the excess
491 protein solution was blotted with filter paper. Ten µL of 2% uranyl acetate were then applied to the grid
492 twice for two 30-second stainings followed by blotting. The grids were air-dried for 5 minutes and
493 visualized by Thermo Fischer F200Ci electron microscope at 120 keV.

494

495 Cryo-EM grids preparation and images acquisition for apo-GLS2

496 Four µL of 5 µM GLS2 were applied to plasma-cleaned grids (300 mesh UltraAu Foil R1.2/1.3, Electron
497 Microscopy Sciences, EMS) for a 30-second incubation. The excess solution was blotted for 4-6 seconds

with filter paper by a Vitrobot mark IV (Thermo Fischer Scientific). Grids were subsequently vitrified in liquid ethane and stored in liquid nitrogen. Cryo-EM single particle micrographs of apo-GLS2 were collected on a Talos Arctica (Thermo Fischer Scientific) at the Cornell Center for Materials Research. The microscope was operated at 200 keV at 63,000x nominal magnification using a Gatan K3 direct electron camera in super-resolution mode, with a Gatan GIF Quantum LS Imaging energy filter, corresponding to a physical pixel size of 1.23 Å/pix. Given the orientation bias of the sample, a non-tilted dataset of 1,171 images and a 30-degree tilted dataset of 488 images were collected and merged for further data processing. The images were obtained with a defocus range of -0.8 to -2.0 um by EPU (Thermo Fischer Scientific). Each stack movie was recorded with 50 frames for a total dose of ~50 e-/Å^2.

Cryo-EM grids preparation and images acquisition for GLS2 (K253A) filament

Human GLS2 (K253A), 3 µM, was mixed with 20 mM glutamine to initiate filament formation. The mixture was applied to plasma-cleaned grids (300 mesh Quantifoil Au R1.2/1.3, EMS) for 30-second incubations. The excess solution was blotted for 5-7 seconds with filter paper by a Vitrobot mark IV. Grids were subsequently vitrified in liquid ethane and stored in liquid nitrogen. Cryo-EM single particle micrographs of apo-GLS2 were collected on a Titan Krios (Thermo Fischer Scientific) at The New York Structural Biology Center. The microscope was operated at 300 keV at 81,000x nominal magnification using a Gatan K3 direct electron camera in counting mode, corresponding to a physical pixel size of 1.058 Å/pix. Thirty-eight hundred and four images were obtained with a defocus range of -0.8 to -2.0 µm by Leginon[41]. Each stack movie was recorded with 40 frames for a total dose of ~50 e-/Å^2.

Cryo-EM data processing

For the apo-GLS2 map, dose-fractionated image stacks were subjected to motioncor2 wrapped in RELION 4.0.0. [42-44] through SBGrid, followed by patch CTF estimation in CryoSPARC V4.0.0. [45]. The motion-corrected micrographs with CTF better than 4 Å were passed for later processing. A blob picker in CryoSPARC was used to generate the templates for further Topaz picking[46], where ~1M particles were picked. The particles were subjected to 3D classification and heterogenous refinement, and only the best classes were kept. The remaining ~329K particles were subjected to homogenous and heterogenous refinement. The final reconstruction with C2 symmetry yields a map with a resolution of 3.12 Å determined by FSC. The workflow is provided in Fig. S6. Cryo-EM maps are visualized in ChimeraX[47].

For the GLS2 (K253A) filament structure, dose-fractionated image stacks were subjected to patch motion correction, followed by patch CTF estimation in CryoSPARC V4.0.0. The motion-corrected micrographs with CTF better than 4 Å were passed for later processing, which yielded 3,640 micrographs. Manual picking in CryoSPARC was used on 40 micrographs to pick ~600 particles manually, which yielded five classes of templates by 2D classification. The selected template was used for the filament trace job in CryoSPARC to template pick particles. Three hundred and thirty three particles were extracted and subjected to 3D classification. The best ~48k particles were reconstructed and refined to yield a 3.3 Å map determined by FSC. The workflow is provided in Fig S7.

Model building and refinement

The initial apo-GLS2 model was adapted from the PDB entry 4BQM for the catalytic domain and 5U0K for the ankyrin repeats. First, both models were manually docked into the map by UCSF ChimeraX. Next, the model was fitted into the map by ISOLDE for the overall adjustment[48], then underwent multiple rounds of automatic refinement using Phenix real space refinement[49], and manual building using Coot[50]. Finally, validation was performed with MolProbity[51]. The final refinement statistics is provided in Table S1.

Data and code availability

The cryo-EM density maps and the atomic model for both apo-GLS2 and the GLS2 (K253A) filament structure reported in this paper have been deposited in EM Data Bank (EMDB: EMD-xxxxx, EMD-xxxxx) and the Protein Data Bank (PDB: XXXX, XXXX), respectively.

ACKNOWLEDGMENTS

We thank Drs. Katherine Spoth, Mariena Silvestry-Ramos, Kasahun Neselu, and Edward Eng for help with EM instrumentation. We would also like to thank Drs. Brian R. Crane, Sekar Ramachandran, and Shawn. K. Milano, for the helpful feedback on the structural analysis. This work was supported by grants from the NIH (R35GM122575 and R01CA201402). The acquisition of the human apo-GLS2 and mouse GAC (Y471W) structures used the Cornell Center for Materials Research Shared Facilities, which is supported by NSF (DMR- 1719875). The collection of negative-stain images relied on using an instrument supported by the NIH through award S10OD030470-01. The acquisition of the GLS2 (K253A) structure was performed at the National Center for CryoEM Access and Training (NCCAT) and the Simons Electron Microscopy Center located at the New York Structural Biology Center, supported by the NIH Common Fund Transformative High-Resolution Cryo-Electron Microscopy program (U24 GM129539) and by grants from the Simons Foundation (SF349247) and NY State Assembly.

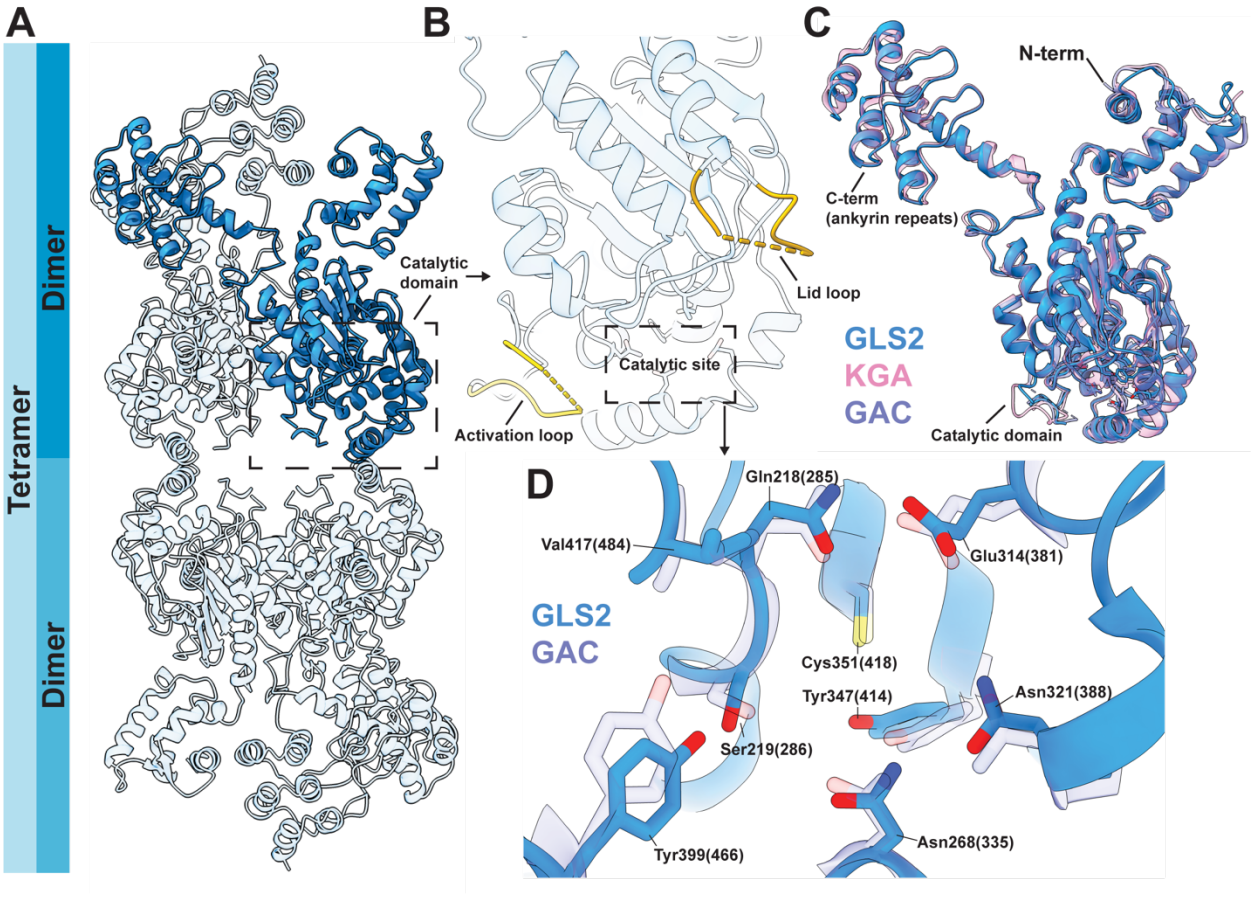
A
Tetramer
Dimer
Dimer
B
Catalytic domain
Lid loop
Catalytic site
Activation loop
C
N-term
C-term (ankyrin repeats)
GLS2
KGA
GAC
Catalytic domain
D
GLS2
GAC
Gln218(285)
Val417(484)
Glu314(381)
Cys351(418)
Tyr347(414)
Asn321(388)
Ser219(286)
Asn268(335)
Tyr399(466)

565
566

Figure 1. The cryo-EM structure of human full-length apo-GLS2 and its comparison with the X-ray crystal structures of the GLS isoforms.

(A) The overall cryo-EM tetrameric structure of human apo-GLS2 consists of two identical dimers. One of the representative monomer subunits is dark blue while the other three subunits are light blue. (B) Zoom-in of the catalytic domain (dashed box in (A)). The positions of the activation loop (light yellow), the catalytic site (dashed box) and the lid loop (dark yellow) are highlighted. The unmodeled region of the activation loop and the lid loop are connected by dashed lines, which represent the flexibility of the loops. (C) The comparison of the GLS2 monomer with that of GLS isoforms KGA (PDB ID: 5UQE, magenta) and GAC (PDB ID: 5D3O, purple). All three glutaminase enzymes exhibit a similar overall folding pattern consisting of an N-terminal region, a highly conserved catalytic domain, and a C-terminal region in which GAC lacks the ankyrin repeats present in GLS2 and KGA. (D) The comparison of the catalytic residues of GLS2 and GAC. The catalytic residues in both glutaminase enzymes are conserved. The numbering of the residues is based on human GLS2 (LGA), while the corresponding human GAC numbering is in parentheses.

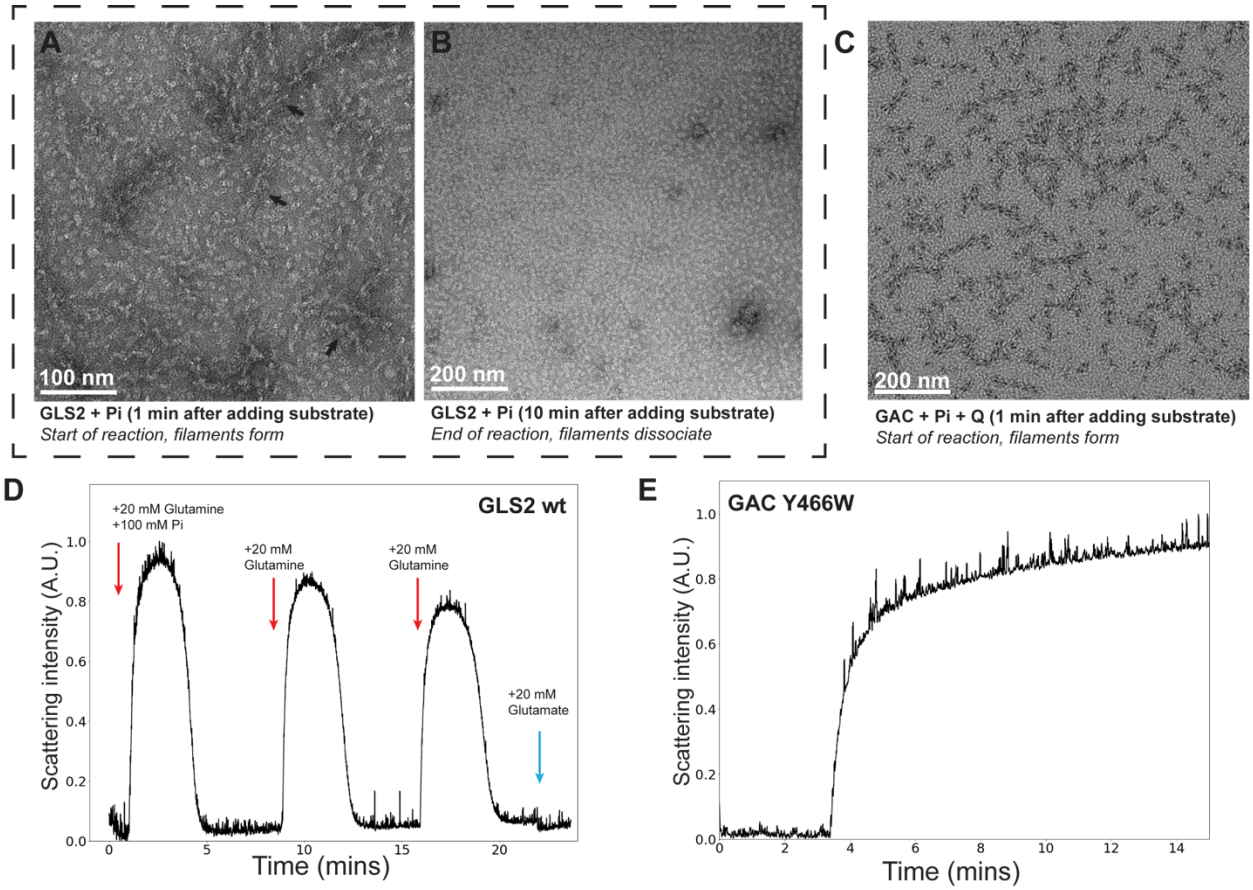
A
100 nm
GLS2 + Pi (1 min after adding substrate)
Start of reaction, filaments form
B
200 nm
GLS2 + Pi (10 min after adding substrate)
End of reaction, filaments dissociate
C
200 nm
GAC + Pi + Q (1 min after adding substrate)
Start of reaction, filaments form
D
GLS2 wt
+20 mM Glutamine
+100 mM Pi
+20 mM
Glutamine
+20 mM
Glutamine
+20 mM
Glutamate
Scattering intensity (A.U.)
Time (mins)
E
GAC Y466W
Scattering intensity (A.U.)
Time (mins)

581
582

583 Figure 2. The formation of the glutaminase filaments is directly coupled to catalytic activity.
584 (A) Representative negative-stain EM images showing the GLS2 filaments that form in the presence of the
585 activator inorganic phosphate (Pi) (50 mM) and 1 minute after the substrate (glutamine; 20 mM) is added
586 (indicated by black arrows). (B) GLS2 filaments dissociate ten minutes after substrate is added,
587 corresponding to the end of the reaction. The concentration of GLS2 in (A) and (B) is 1 μM. The images
588 were obtained using a Thermo Fisher F200i at 120 KeV. (C) Representative negative-stain EM images
589 showing the GAC (1 mM) filaments that form in the presence of Pi (50 mM) and 1 minute after the addition
590 of glutamine (20 mM). (D) Right-angle light scattering GLS2 (2 μM) profiles after the addition of glutamine
591 (20 mM) plus Pi (50 mM), or glutamate alone. The addition of glutamate (product) alone does not induce
592 filaments to form. (E) Right-angle light scattering profile of the human GAC (Y466W) mutant that binds
593 substrate but is catalytically-defective. Filaments form when GAC (Y466W) is treated with glutamine and
594 persist due to the lack of catalytic activity. The excitation wavelength and the emission wavelength are
595 both 340 nm. X-axis: time in minutes; Y-axis: the intensity of the scattering, which is proportional to the
596 size of the filaments.

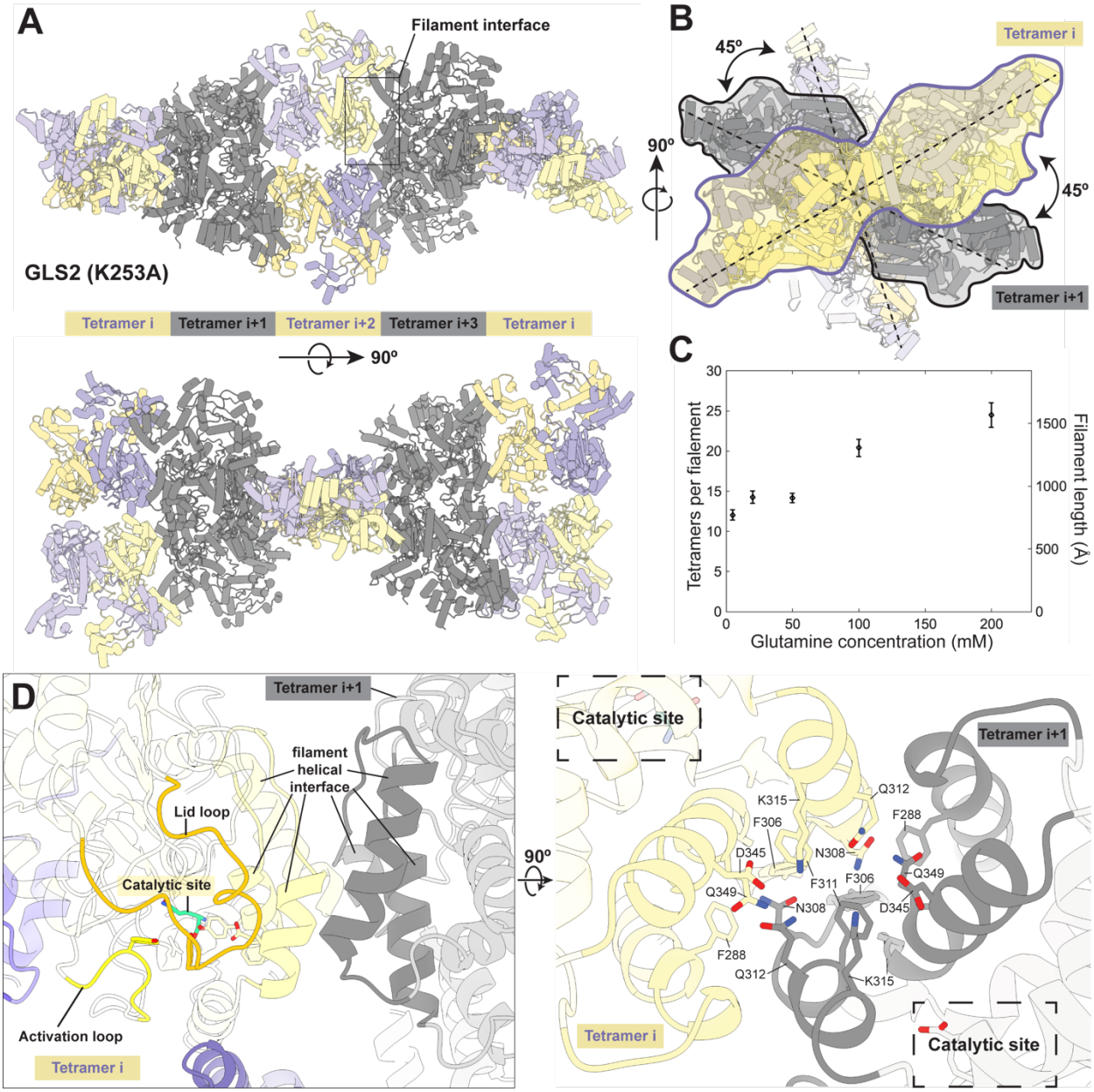
A
Filament interface
GLS2 (K253A)
Tetramer i
Tetramer i+1
Tetramer i+2
Tetramer i+3
Tetramer i
90°
B
Tetramer i
45°
90°
45°
Tetramer i+1
C
Tetramers per fialement
Filament length (Å)
Glutamine concentration (mM)
D
Tetramer i+1
filament
helical
interface
Lid loop
Catalytic site
Activation loop
Tetramer i
90°
Catalytic site
Tetramer i+1
K315
Q312
F288
F306
D345
N308
Q349
F311
F306
Q349
N308
D345
F288
Q312
K315
Tetramer i
Catalytic site

600 Figure 3. The structure of the human GLS2 (K253A) filament captured under catalytic turnover conditions.
601 (A) The structure of the GLS2 (K253A) filament, shown for five tetramers that comprise a representative
602 stretch of this higher-order oligomer. Each tetramer is colored in gray or yellow and purple to allow for
603 distinguishing between the monomeric units that comprise each tetramer. The filament interface is
604 highlighted with a black box and is zoomed in Figure 3D. (B) The structure of the GLS2 (K253A) filament
605 viewed down the filament axis. The first and the second tetramers are outlined with purple and black
606 silhouettes, respectively. The dashed line indicates the longest dimension of each tetramer and highlights
607 the 45° rotation around the filament axis between adjacent tetramers. (C) The average number of
608 tetramers per filament plotted against substrate (glutamine) concentration. The filament length was
609 determined through an analysis of negative-stain electron microscopy images with ImageJ. The width of
610 each GLS2 tetramer is 64 Å, as measured from the high resolution cryo-EM structure of the GLS2 filament.
611 X-axis: the concentration of substrate (glutamine) in mM; left Y-axis: the number of tetramers per
612 filament; right Y-axis: the average length of filaments in Å. Error bars are shown for the standard error.
613 (D) Each interface between the tetrameric units of the filament consists of six alpha helices, three from
614 each adjacent tetramer. Left: Figure depicting the positions of the helical interfaces, the activation loop,
615 the catalytic site, and the lid loop (in orange). The adjacent tetramer is colored gray, and the six alpha
616 helices forming the interface are in solid colors. Right: The interaction network at a helical interface
617 between tetramers comprising the filament. The catalytic site is highlighted with a dashed box to
618 demonstrate the close proximity of each helical interface and enzyme active site.
619

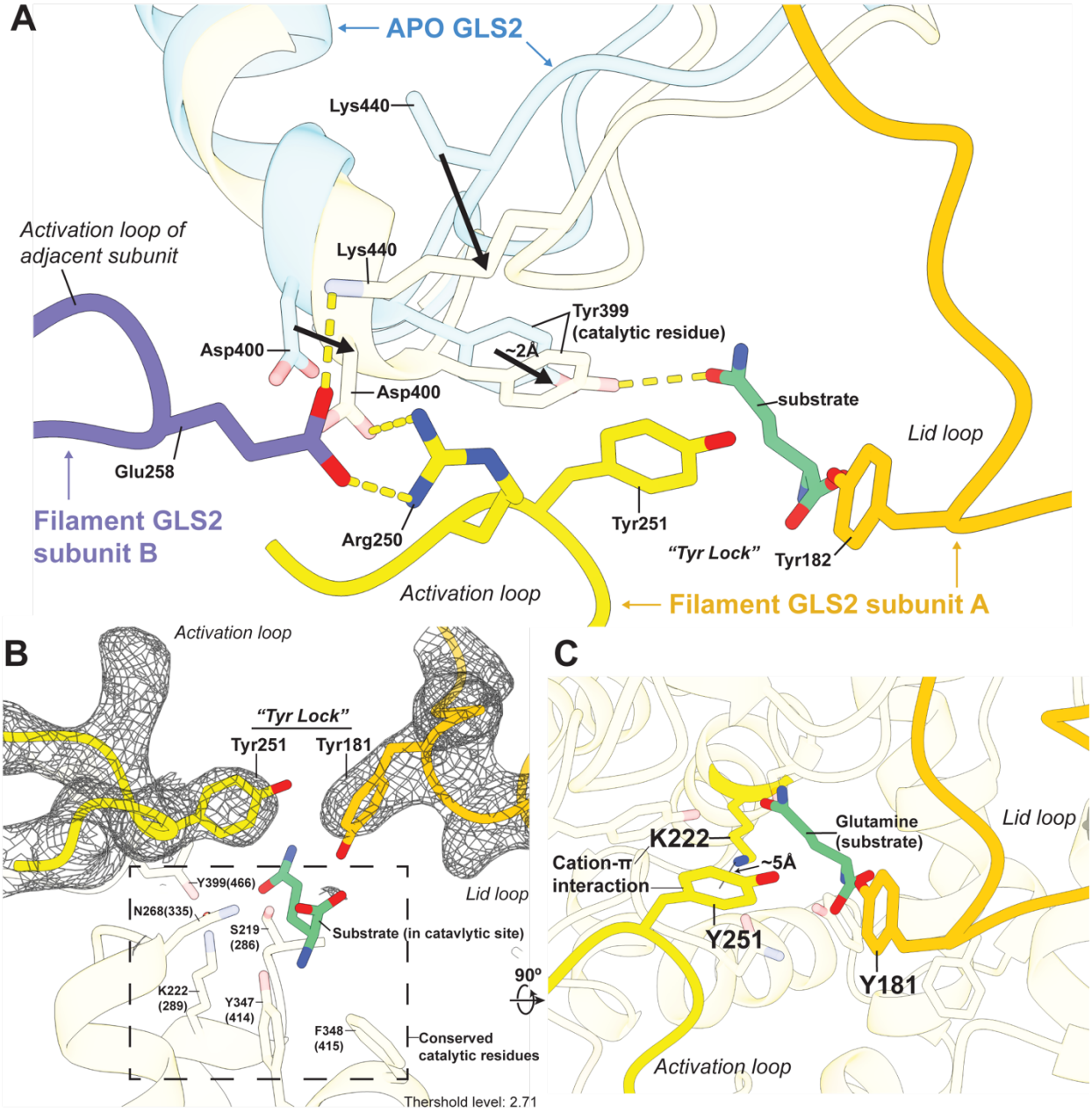
A
APO GLS2
Lys440
Activation loop of adjacent subunit
Lys440
Tyr399 (catalytic residue)
Asp400
~2Å
Asp400
substrate
Lid loop
Glu258
Filament GLS2 subunit B
Arg250
Tyr251
"Tyr Lock"
Tyr182
Activation loop
Filament GLS2 subunit A
B
Activation loop
"Tyr Lock"
Tyr251
Tyr181
Y399(466)
N268(335)
S219 (286)
Substrate (in catavlytic site)
Lid loop
K222 (289)
Y347 (414)
F348 (415)
Conserved catalytic residues
Thershold level: 2.71
90°
C
Lid loop
K222
Glutamine (substrate)
Cation-π interaction
~5Å
Y251
Y181
Activation loop

620
621

Figure 4. The structure of the GLS2 filament reveals allosteric conformational changes within the GLS2 tetrameric units during catalysis.

(A) The conformation of the activation loop within each enzyme subunit (designated subunits A and B) comprising the GLS2 filament induces an allosteric conformational change resulting in the insertion of the catalytic residue Tyr399 into the active site. Apo-GLS2 is light blue, and the GLS2 filament is shown in purple (an activation loop from an adjacent subunit), light yellow, darker yellow (an activation loop), and orange (lid loop). Interactions between key residues, consisting of hydrogen bonds and salt bridges, are shown as dashed lines in medium yellow. The arrows indicate the direction of the conformational changes occurring within the GLS2 filament relative to apo-GLS2. (B) The tyrosine lock packs the substrate in a preferred conformation against catalytic residues. The locations of conserved catalytic residues are indicated with lines, and the electron densities of the activation loop and the lid loop are shown as mesh. (C) The tyrosine lock consisting of Tyr251 from the activation loop (yellow) and Tyr181 from the lid loop (orange). The substrate, glutamine, is shown in green. Lys222 performs the first step in catalysis, which is enhanced by its interaction with Tyr251 from the activation loop through a cation-π interaction.

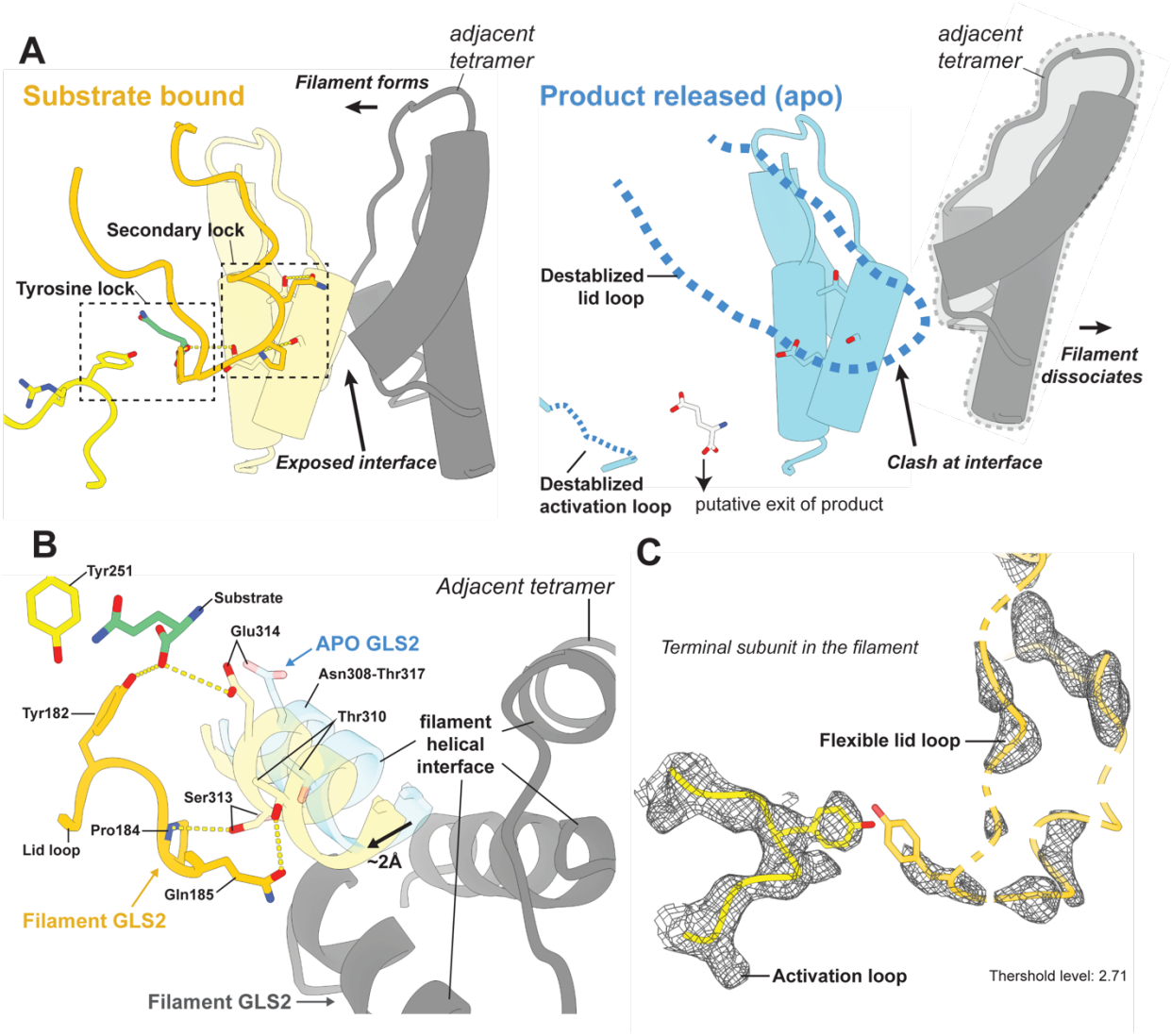
A
Substrate bound
adjacent tetramer
Filament forms
Secondary lock
Tyrosine lock
Exposed interface
Product released (apo)
adjacent tetramer
Destablized lid loop
Filament dissociates
Clash at interface
Destablized activation loop
putative exit of product
B
Tyr251
Substrate
Adjacent tetramer
Glu314
APO GLS2
Asn308-Thr317
Tyr182
Thr310
filament helical interface
Ser313
Pro184
Lid loop
~2Å
Gln185
Filament GLS2
Filament GLS2
C
Terminal subunit in the filament
Flexible lid loop
Activation loop
Thershold level: 2.71

637
638

Figure 5. The proposed mechanism of glutaminase filament formation and dissociation.
(A) The proposed mechanism for glutaminase filament formation and dissociation. Left: When substrate is bound, the lid (in orange) is stabilized by the secondary lock and the helical interface is exposed for an adjacent tetramer within the filament (shown in gray) to bind. Right: When product is released, the lid loop becomes flexible, displacing the adjacent tetramer, and blocking the helical interface that would have formed between two tetrameric units. (B) The lid loop (orange) in the GLS2 filament is stabilized in the active conformation through a secondary lock involving the lid loop with residues adjacent to the helical interface that forms between two tetrameric units within the filament structure. The adjacent tetramer that is forming the helical interface is shown in gray. Hydrogen bonds are indicated with yellow dashed lines. Apo-GLS2 is light blue and the GLS2 filament is shown in yellow and orange. The arrow indicates the direction of the conformational change. (C) The cryo-EM density map of the lid loop of the terminal subunit in the GLS2 filament. The weak density of the lid loop in the terminal tetramer suggests increased flexibility in comparison to the other tetramers making up the filament, which display strong density for the lid loop as depicted in Figure 4B.

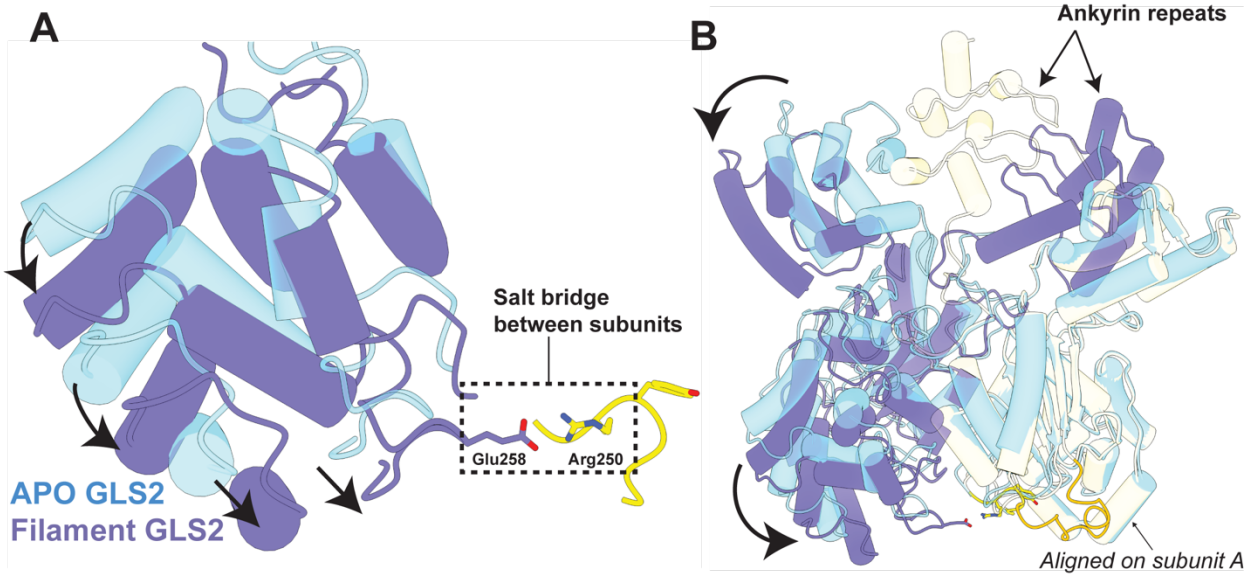
A
Salt bridge
between subunits
Glu258
Arg250
APO GLS2
Filament GLS2
B
Ankyrin repeats
Aligned on subunit A

655
656

657 Figure 6. The proposed mechanism for regulation of GLS2 catalytic activity by the C-terminal ankyrin
658 repeats.
659 (A) The ankyrin repeats in the GLS2 filament structure (purple) undergo a movement that enables the
660 formation of a salt bridge between adjacent subunits within a tetrameric unit that stabilizes the activation
661 loop. The arrow indicates the direction of conformational changes. Apo-GLS2 is shown in light blue and
662 the GLS2 filament is in purple and yellow. (B) A dimeric unit of the GLS2 filament (purple, light and darker
663 yellow) and a dimeric unit of apo-GLS2 (light blue) are shown. The presence of the ankyrin repeats within
664 apo-GLS2 would appear to block the movements that enable the salt bridge between Glu258 and Arg250
665 to form which is necessary for maximal catalytic activity. Apo-GLS2 is aligned against the monomeric
666 subunit of the GLS2 filament dimer in light yellow. Also, see supplementary movie 1.
667
668

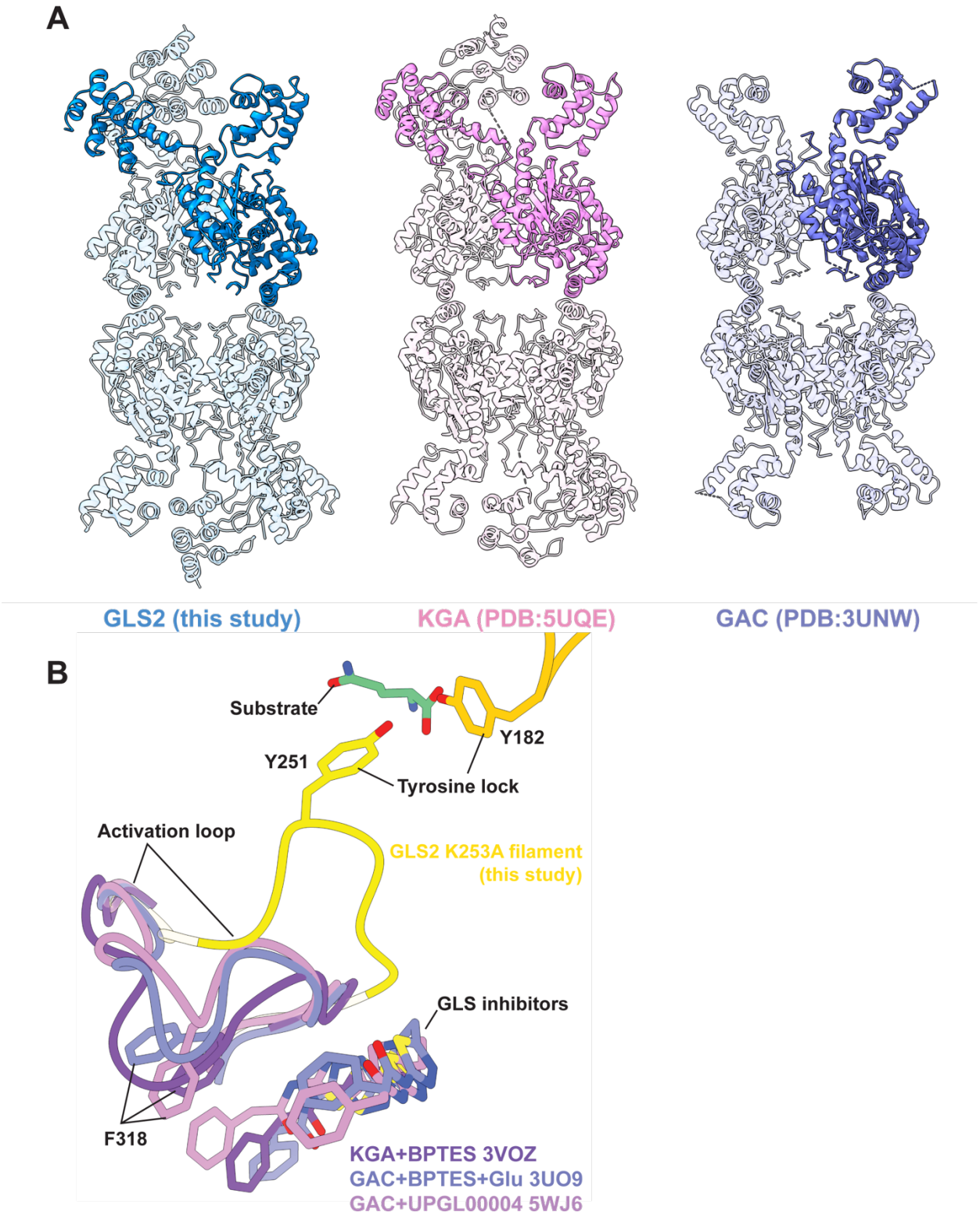
A
GLS2 (this study)
KGA (PDB:5UQE)
GAC (PDB:3UNW)
B
Substrate
Y182
Y251
Tyrosine lock
Activation loop
GLS2 K253A filament
(this study)
GLS inhibitors
F318
KGA+BPTES 3VOZ
GAC+BPTES+Glu 3UO9
GAC+UPGL00004 5WJ6

669
670

671 Figure S1. (A) The comparison of the structures of GLS2, KGA and GAC (from left to right). All three
672 structures show the enzymes as tetramers. One of the representative subunits in each tetramer is
673 highlighted in solid color. (B) The comparison of the activation loops between the GLS2 (K253A) filament
674 (yellow) and GAC bound to the allosteric inhibitors BPTES, alone or together with glutamate, and
675 UPGL0004 (purple, lavender and pink, respectively).
676

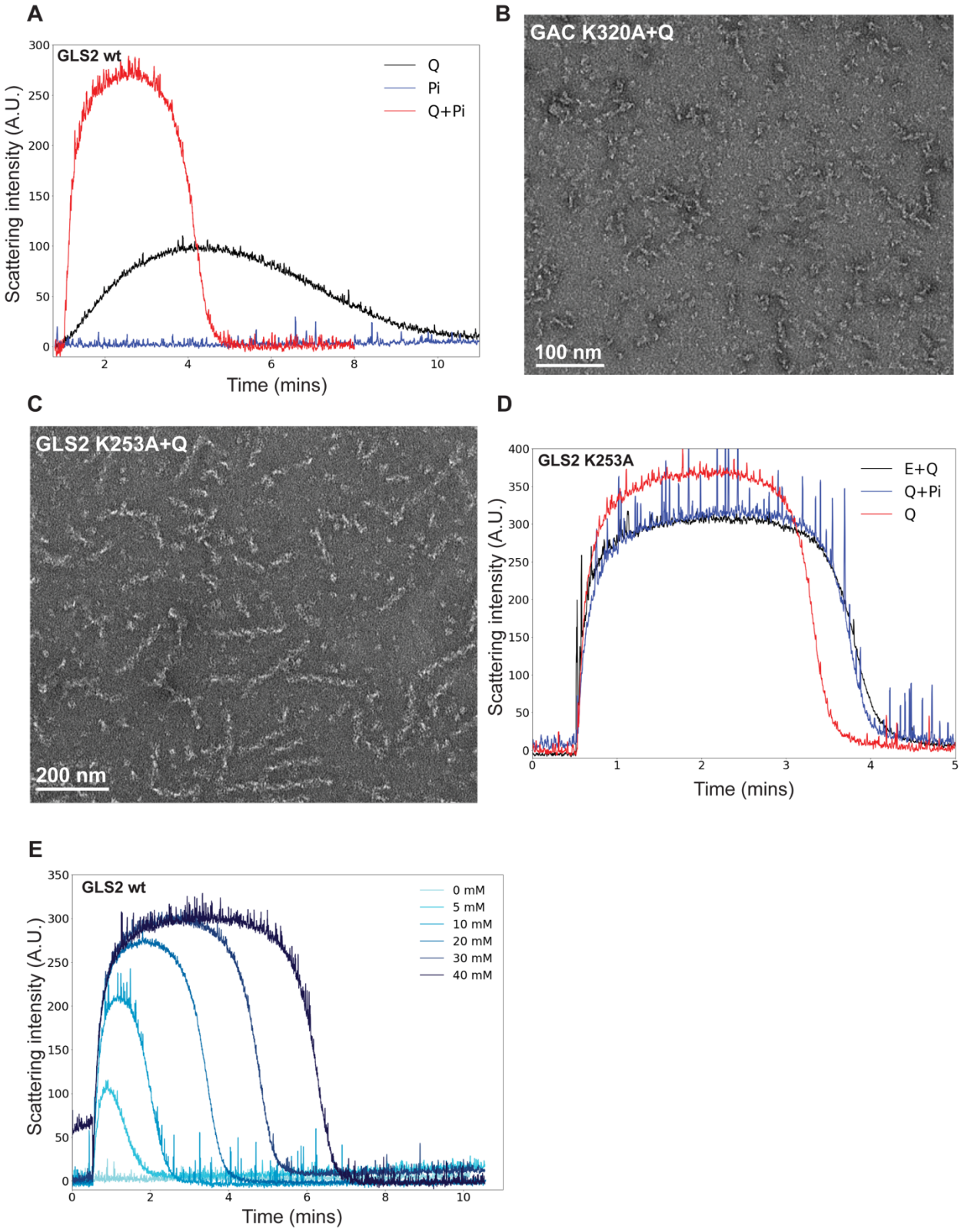
A
GLS2 wt
Q
Pi
Q+Pi
Scattering intensity (A.U.)
Time (mins)
B
GAC K320A+Q
100 nm
C
GLS2 K253A+Q
200 nm
D
GLS2 K253A
E+Q
Q+Pi
Q
Scattering intensity (A.U.)
Time (mins)
E
GLS2 wt
0 mM
5 mM
10 mM
20 mM
30 mM
40 mM
Scattering intensity (A.U.)
Time (mins)

677

678 Figure S2. (A) RALS profile of wildtype GLS2 (2 μM) shows that phosphate (Pi)(50 mM) enhances filament
679 formation relative to the addition of glutamine (designated as Q)(20 mM) or phosphate alone. (B) The
680 representative negative-stain EM images of the constitutively active GAC (K320A) filaments that form
681 upon substrate addition. (C) The representative negative-stain EM images of the constitutively active GLS2
682 (K253A) filaments that form upon substrate addition. (D) The RALS profiles of GLS2 (K253A) (2 μM)
683 filament formation. Glutamine (designated as Q)(20 mM) stimulates filament formation, whereas
684 glutamate, alone, (designated as E)(20 mM) does not (black trace). The addition of excess glutamate prior
685 to the addition of glutamine has no effect on the ability of glutamine to in duce filament formation (black
686 trace). Blue and red traces show that the constitutively active GLS2 (K253A) mutant is insensitive to the
687 addition of inorganic phosphate (Pi)(50 mM). (E) Changes in GLS2 filament size as a function of glutamine
688 concentration (listed in upper right in the figure). Filaments are larger and are more sustained in the
689 presence of higher concentrations of substate.
690

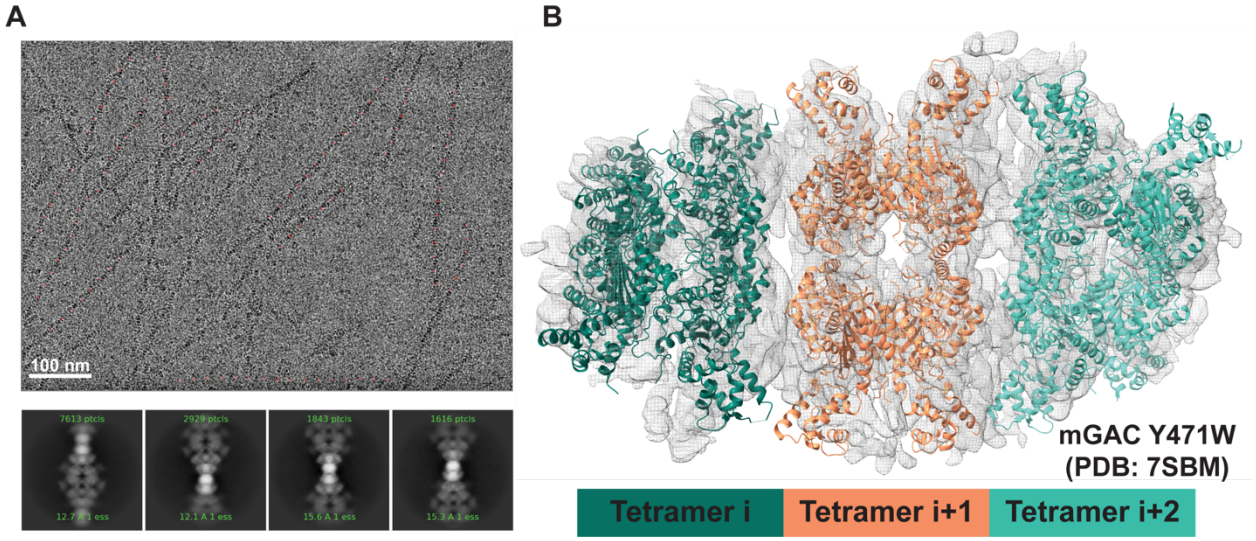
A
100 nm
7613 ptcls
2929 ptcls
1843 ptcls
1616 ptcls
12.7 A 1 ess
12.1 A 1 ess
15.6 A 1 ess
15.3 A 1 ess
B
mGAC Y471W
(PDB: 7SBM)
Tetramer i
Tetramer i+1
Tetramer i+2

691

692 Figure S3. (A) Representative cryo-EM micrographs of the mouse GAC (Y471W) filament and the
693 corresponding 2D classes. (B) The cryo-EM 3D reconstruction of the mouse GAC (Y471W) filament at a
694 resolution of ~6 Å. The Y471W mutant in the mouse has identical properties to the Y466W mutant in
695 human GAC. Three tetramers are shown as a part of the filament, with each tetramer shown in a different
696 color. The X-ray crystal structure for (GAC Y466W) is docked on to the map (PDB: 7SBM). Note that mouse
697 GAC (Y471W) filament assembly is similar to that for human GLS2 (K253A).
698

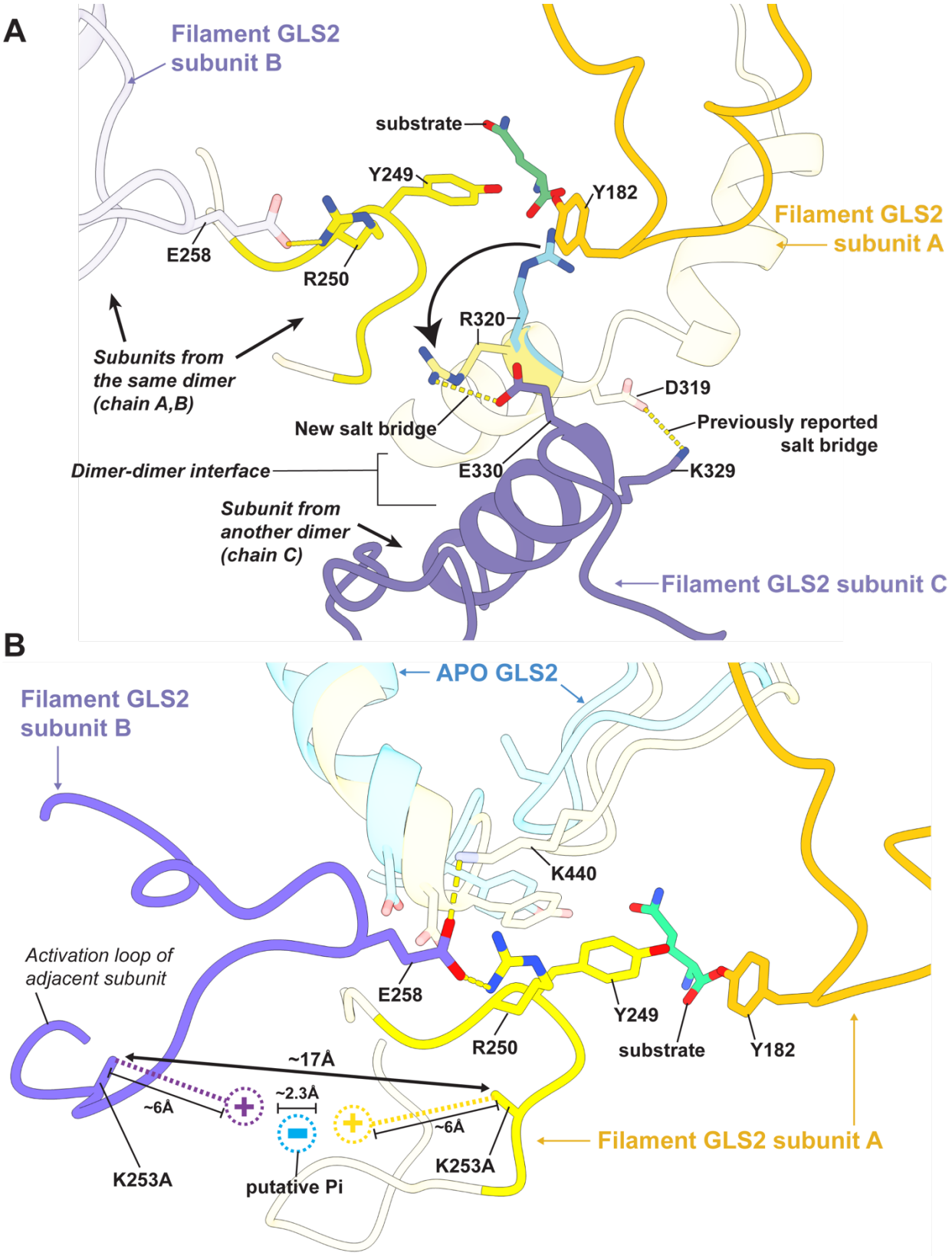
A
Filament GLS2 subunit B
substrate
Y249
Y182
Filament GLS2 subunit A
E258
R250
R320
Subunits from the same dimer (chain A,B)
D319
New salt bridge
Previously reported salt bridge
Dimer-dimer interface
E330
K329
Subunit from another dimer (chain C)
Filament GLS2 subunit C
B
APO GLS2
Filament GLS2 subunit B
K440
Activation loop of adjacent subunit
E258
Y249
R250
substrate
Y182
~17Å
~6Å
~2.3Å
~6Å
Filament GLS2 subunit A
K253A
putative Pi
K253A

699

700 Figure S4. (A) The new salt bridge that forms between Arg320 and Glu330 from adjacent dimers (subunits
701 A and C) within a tetrameric unit of the constitutively active GLS2 (K253A) filament, together with the
702 previously reported interaction between the corresponding residues in GAC, namely Asp319 and Lys329
703 [30], enhances tetramer formation. Arg320 is located near catalytic pocket in apo-GLS2, which is displaced
704 by Tyr182 from the tyrosine lock (orange) in the GLS2 (K253A) filament, as shown by the arrow. The light
705 purple activation loop on the top left is from the adjacent subunit B of the same dimer within a tetrameric
706 unit as the yellow subunit A, and the darker purple activation loop on the bottom from subunit C is from
707 a distinct dimer. (B) The putative position of inorganic phosphate (Pi) as activator in wild type GLS2. The
708 position of positive-charged side chains of Lys253 in subunits A and B are possibly stabilized by the
709 negative-charged phosphate (Pi).
710

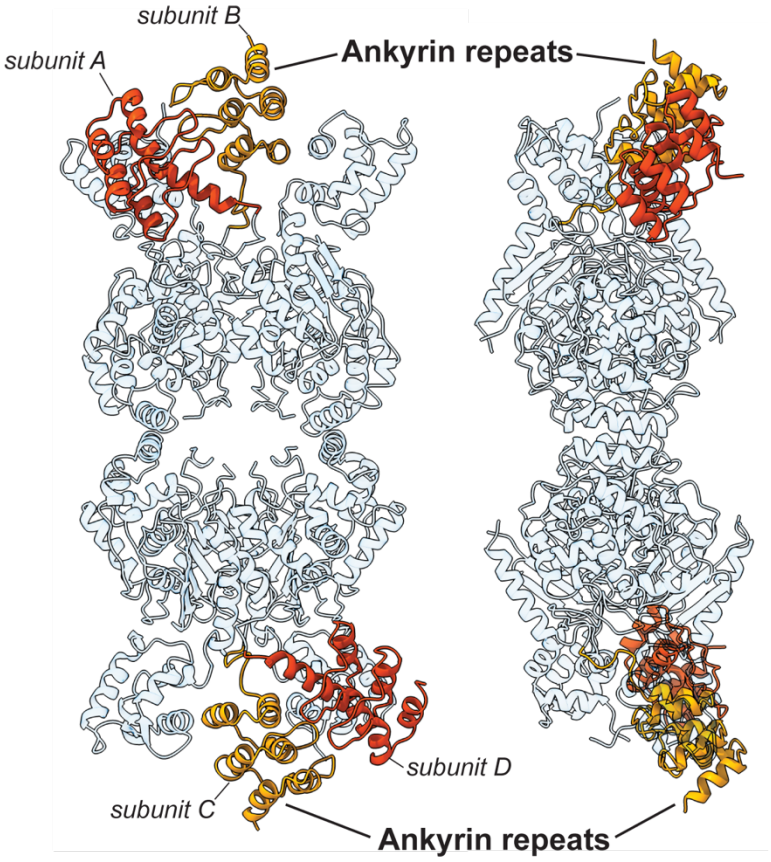
subunit B
subunit A
Ankyrin repeats
subunit D
subunit C
Ankyrin repeats

711

712 Figure S5. The asymmetric positions of the apo-GLS2 ankyrin repeats from different subunits shown in
713 orange and yellow.
714

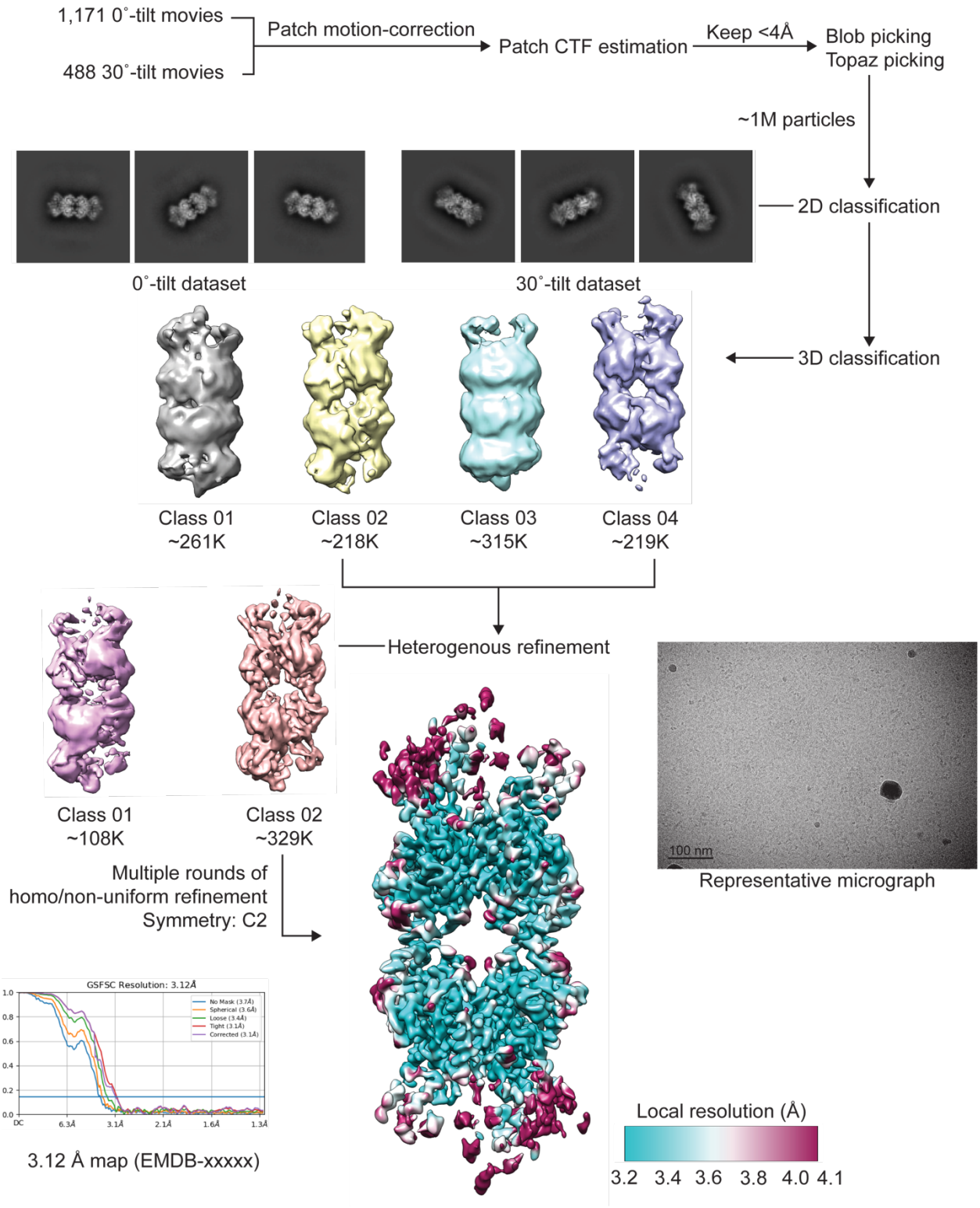
1,171 0˚-tilt movies
488 30˚-tilt movies
Patch motion-correction
Patch CTF estimation
Keep <4Å
Blob picking
Topaz picking
~1M particles
2D classification
0˚-tilt dataset
30˚-tilt dataset
3D classification
Class 01
~261K
Class 02
~218K
Class 03
~315K
Class 04
~219K
Heterogenous refinement
Class 01
~108K
Class 02
~329K
Multiple rounds of
homo/non-uniform refinement
Symmetry: C2
100 nm
Representative micrograph
GSFSC Resolution: 3.12Å
No Mask (3.7Å)
Spherical (3.6Å)
Loose (3.4Å)
Tight (3.1Å)
Corrected (3.1Å)
DC
6.3Å
3.1Å
2.1Å
1.6Å
1.3Å
3.12 Å map (EMDB-xxxxx)
Local resolution (Å)
3.2 3.4 3.6 3.8 4.0 4.1

717 Figure S6. The cryo-EM data processing workflow of apo-GLS2.
718

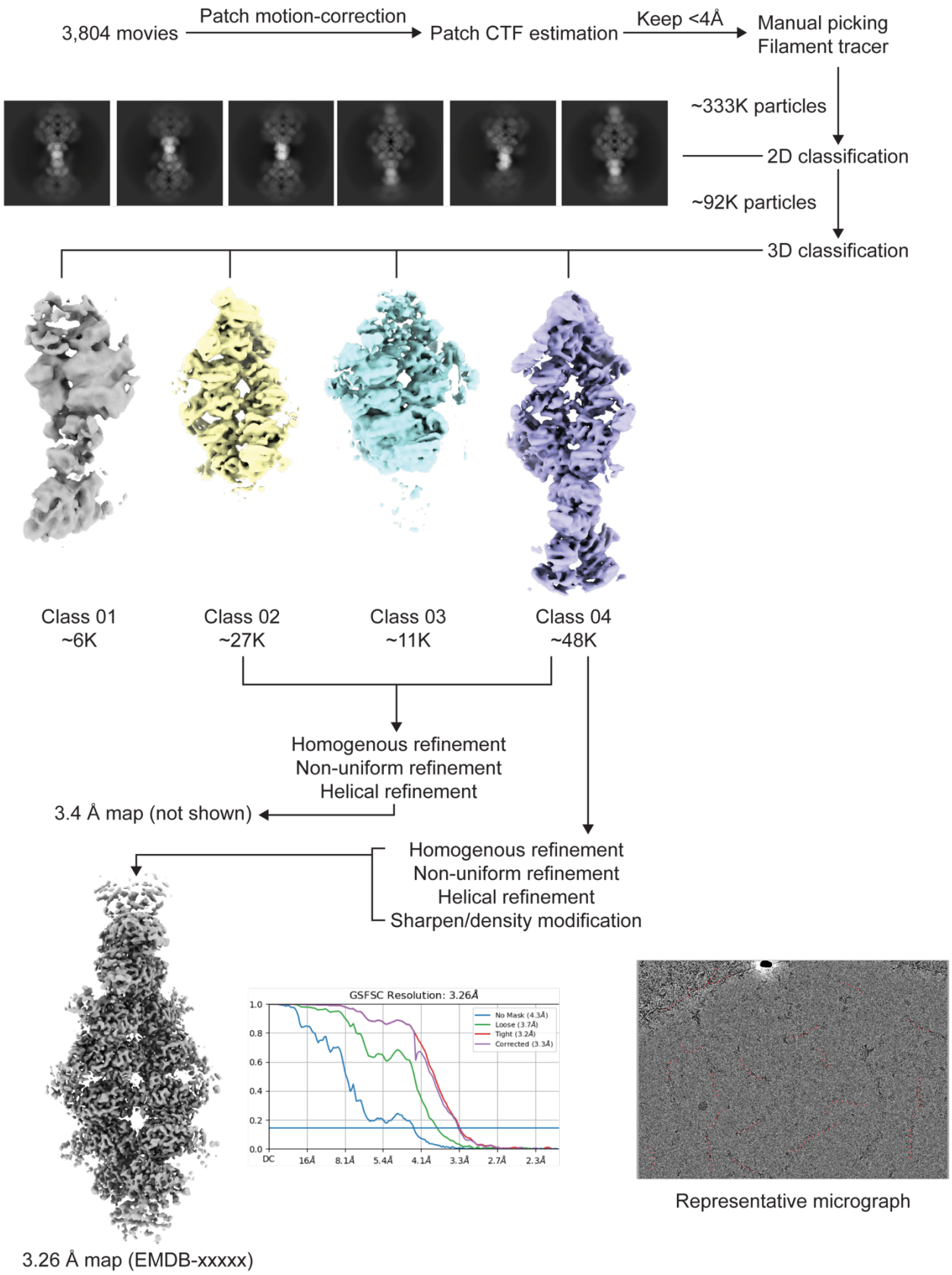
3,804 movies
Patch motion-correction
Patch CTF estimation
Keep <4Å
Manual picking
Filament tracer
~333K particles
2D classification
~92K particles
3D classification
Class 01
~6K
Class 02
~27K
Class 03
~11K
Class 04
~48K
Homogenous refinement
Non-uniform refinement
Helical refinement
3.4 Å map (not shown)
Homogenous refinement
Non-uniform refinement
Helical refinement
Sharpen/density modification
GSFSC Resolution: 3.26Å
No Mask (4.3Å)
Loose (3.7Å)
Tight (3.2Å)
Corrected (3.3Å)
1.0
0.8
0.6
0.4
0.2
0.0
DC
16Å
8.1Å
5.4Å
4.1Å
3.3Å
2.7Å
2.3Å
Representative micrograph
3.26 Å map (EMDB-xxxxx)

719

720 Figure S7. The cryo-EM data processing workflow of GLS2 K253A filament.
721

722 **Table S1. Cryo-EM data collection, refinement and validation statistics**

723

	Apo GLS2 (EMDB-xxxx) (PDB xxxx)	GLS2 K253A filament (EMDB-xxxx) (PDB xxxx)
Data collection and processing		
Magnification	63kx	81kx
Voltage (kV)	200	300
Electron exposure (e–/Å^2)	50	50
Defocus range (μm)	-0.8~-2.0	-0.8~-2.0
Physical pixel size (Å)	1.23	1.058
Symmetry imposed	C2	C1
Initial particle images (no.)	~1M	~333K
Final particle images (no.)	~329K	~49K
Map resolution (Å)	3.12	3.26
FSC threshold	0.143	0.143
Map resolution range (Å)	3.0-5.0	3.0-5.0
Refinement		
Initial model used (PDB code)	4BQM	4BQM
Model resolution (Å)	3.12	3.26
FSC threshold	0.143	0.143
Model resolution range (Å)	3.0-5.0	3.0-5.0
Map sharpening *B* factor (Å^2)	147.25	211.56
Model composition		
Non-hydrogen atoms	15,496	15,642
Protein residues	2016	2032
Ligands	0	4
B factors (Å^2)	147.25	211.56
Protein	147.25	211.56
Ligand		
R.m.s. deviations		
Bond lengths (Å)	0.004	0.004
Bond angles (°)	0.710	0.747
Validation		
MolProbity score	2.05	1.88
Clashscore	13.51	9.63
Poor rotamers (%)	0.12	0.77
Ramachandran plot		
Favored (%)	93.75	94.54
Allowed (%)	6.25	5.16
Disallowed (%)	0.00	0.30

724